Monthly Notices of the ROYAL ASTRONOMICAL SOCIETY

MNRAS **548,** 1–17 (2026) https://doi.org/10.1093/mnras/stag766
Advance Access publication 2026 April 23

Growing in number, passive in nature: tracing the evolution of the most massive quiescent galaxies since $z \sim 0.8$ with BOSS and DESI

F. R. Ditrani [1,2]★ M. Fossati [1,2] M. Longhetti,[2] F. La Barbera,[3] A. Iovino,[2] C. Maraston,[4] D. Thomas[5,6] and D. Bevacqua [7]

[1]*Università degli studi di Milano-Bicocca, Piazza della scienza, I-20125 Milano, Italy*
[2]*INAF – Osservatorio Astronomico di Brera, Via Brera 28, I-20121 Milano, Italy*
[3]*INAF – Osservatorio Astronomico di Capodimonte, Via Moiariello 16, I-80131 Napoli, Italy*
[4]*Institute of Cosmology, University of Portsmouth, Burnaby Road, Portsmouth PO1 3FX, UK*
[5]*School of Mathematics and Physics, University of Portsmouth, Lion Gate Building, Portsmouth PO1 3HF, UK*
[6]*School of Physics and Astronomy, University of Leeds, Leeds LS2 9JT, UK*
[7]*INAF – Osservatorio Astronomico di Roma, Via Frascati 33, I-00078 Monte Porzio Catone, Italy*

Accepted 2026 April 21. Received 2026 March 23; in original form 2025 December 23

ABSTRACT

Luminous red galaxies (LRGs) are among the most massive galaxies at any epoch, and lack ongoing star formation. As systems hosting most of the baryonic mass in the local Universe, they preserve imprints of the quenching mechanisms in the early Universe. We exploited the large BOSS and DESI spectroscopic data sets to perform the first homogeneous and continuous mapping of the evolution of stellar population properties of a complete sample of the most massive LRGs ($\log(M_*/\mathrm{M}_\odot) > 11.5$) at $0.15 < z < 0.8$. By consistently fitting the same spectral indices at all redshifts, we measured trends of [Fe/H], [α/Fe], and light-weighted age as a function of redshift. These galaxies exhibit a passive light-weighted age evolution and flat [Fe/H] and [α/Fe] trends towards lower redshift, indicating genuinely passive evolution. These trends are robust against the choice of stellar population models and analysis assumptions, and they support the predictions from IllustrisTNG, which predict negligible chemical evolution for the most massive quenched systems at $z \leq 0.8$. Our results suggest that, despite nearly 5 Gyr of cosmic time and a 3−4× increase in number density, the stellar population properties of massive quiescent galaxies remain essentially unchanged since $z \sim 0.8$. This shows a negligible progenitor bias below $z \sim 0.8$, and a genuinely passive evolution. Newly added systems after $z \sim 0.8$ were already largely quenched and chemically mature, while subsequent evolution was dominated by dry mergers without altering the bulk of the stellar populations.

Key words: galaxies: abundances – galaxies: evolution – galaxies: formation – galaxies: stellar content.

1 INTRODUCTION

Luminous red galaxies (LRGs) are a population of massive, quiescent galaxies identified by their high luminosities and red rest-frame optical colours, indicative of a dominant old stellar population. LRGs rank among the most massive galaxies at their epoch ($\log(M_*/\mathrm{M}_\odot) > 11.5$), with no ongoing star formation (e.g. D. J. Eisenstein et al. 2001; T. Barber, A. Meiksin & T. Murphy 2007). The LRGs are highly biased tracers of the overall cosmic matter distribution and thus ideal to study large-scale structures. As the dominant systems hosting the bulk of the baryonic mass in the local Universe (A. Renzini 2006, and references therein), these massive, quiescent galaxies preserve clear fingerprints of the physical processes that quenched star formation in the early Universe, serving as cosmic laboratories for understanding the formation and evolution of massive galaxies (A. Gallazzi et al. 2005; D. Thomas et al. 2005). A powerful way to explore the physical mechanisms of LRG assembly is by tracing their stellar population properties. Tracing their stellar ages, total metallicities, and [α/Fe] abundance ratios offers powerful diagnostics of their star formation histories. The [α/Fe] ratio, and in particular [Mg/Fe], is sensitive to the duration of star formation (B. M. Tinsley 1979; D. Thomas, L. Greggio & R. Bender 1999) because α-elements (such as Mg) are predominantly produced by core-collapse supernovae from massive stars, which explode on short time-scales (∼ 10 Myr). In contrast, the bulk of iron is released later by Type Ia supernovae, which arise from longer-lived progenitors and enrich the interstellar medium on time-scales of ∼ 1 Gyr (L. Greggio & A. Renzini 1983; M. Jafariyazani et al. 2025). As a result, under the assumption of a constant initial mass function (IMF; I. Ferreras et al. 2015; F. Fontanot et al. 2018) a high [Mg/Fe] indicates a short, intense burst of star formation completed before significant iron enrichment could occur (F. Matteucci & A. Tornambe 1987), while lower values point to more extended star formation

★ E-mail: f.ditrani1@campus.unimib.it

© The Author(s) 2026.
Published by Oxford University Press on behalf of Royal Astronomical Society. This is an Open Access article distributed under the terms of the Creative Commons Attribution License (https://creativecommons.org/licenses/by/4.0/), which permits unrestricted reuse, distribution, and reproduction in any medium, provided the original work is properly cited.

Downloaded from academic.oup.com/mnras/article/548/4/stag766/8661535 by guest on 26 November 2026

histories. Combining [Mg/Fe] with age and metallicity estimates allows us to reconstruct both the timing and duration of star formation episodes, thus providing a physically grounded view of galaxy assembly. First statistical studies based on the Sloan Digital Sky Survey (SDSS; D. J. Eisenstein et al. 2001, 2005) have played a key role in understanding the properties of LRGs in the local Universe up to $z < 0.1$. In the local Universe, LRGs exhibit old stellar populations with high stellar metallicity and enhanced α-element abundances relative to iron (D. Thomas et al. 2005; T. Barber et al. 2007; D. Thomas et al. 2010). Going up to $z \sim 0.4$, the Baryon Oscillation Spectroscopic Survey (BOSS; K. S. Dawson et al. 2013; B. Reid et al. 2016) confirmed the properties of LRGs, indicating short and intense star formation episodes at high redshift. The SDSS and BOSS surveys have therefore established a robust observational framework, highlighting the early assembly and passive evolution of LRGs (C. Maraston et al. 2013; K. Bundy et al. 2017). However, these surveys are complete up to $z \sim 0.4$ and in a narrow higher redshift slice ($0.55 < z < 0.6$, A. Leauthaud et al. 2016) for LRGs in the very high mass end ($\log(M_*/\mathrm{M}_\odot) > 11.6$), leaving open key questions about how their stellar populations evolved at earlier epochs.

Intermediate redshifts ($0.4 \leq z \leq 1$) represent a crucial stage in the evolution of LRGs, as at $z \sim 1$ the fraction of quiescent galaxies with $\log(M_*/\mathrm{M}_\odot) > 11.5$ reaches its maximum and increases in number density only slowly at lower redshift (A. Muzzin et al. 2013). This epoch thus marks the point when the majority of the most massive galaxies have completed their stellar mass assembly and transitioned onto the passive sequence. Studying this redshift range is therefore key to understanding how and when massive galaxies settle into the quiescent population observed locally.

Apart from a few smaller studies targeting intermediate-redshift galaxies (e.g. J. Choi et al. 2014; A. Gallazzi et al. 2014), one of the first large statistical spectroscopic surveys in this redshift regime has been the Large Early Galaxy Astrophysics Census (LEGA-C; A. Wel et al. 2016, 2021). LEGA-C allowed detailed measurements of the stellar population properties of massive quiescent galaxies at these intermediate redshifts (e.g. M. Cappellari 2023; F. R. Ditrani et al. 2025), with a few studies concerning the [α/Fe] abundances (e.g. A. G. Beverage et al. 2021; D. Bevacqua et al. 2023; A. G. Beverage et al. 2023). However, LEGA-C targets a single field (COSMOS, N. Scoville et al. 2007) covering only $\sim 1.6\,\mathrm{deg}^2$, and given the low number density of the most massive systems ($\log(M_*/\mathrm{M}_\odot) > 11.5$), the resulting sample contains too few massive quiescent galaxies to enable a statistically robust analysis of their properties. A wider-area spectroscopic survey is therefore required to probe the high-mass end of the quiescent population with sufficient statistics.

Recently, the Dark Energy Spectroscopic Instrument (DESI; DESI Collaboration 2016a, b) is undertaking the largest LRG survey to date. Indeed, it will observe around 8 million LRGs in the redshift range $0.4 < z < 1$, covering around $14\,000\,\mathrm{deg}^2$. Compared to observations from the surveys described above, DESI provides a significantly higher sampling density and extends the coverage to higher redshifts. In particular, the LRG sample achieves a comoving number density of $5 \times 10^{-4} h^3 Mpc^{-3}$, obtaining a complete population of massive quiescent galaxies with $\log(M_*/\mathrm{M}_\odot) > 11.5$ within $0.4 \leq z \leq 1$ (R. Zhou et al. 2023).

In this work, we exploited the extensive spectroscopic data sets from the BOSS and DESI surveys to carry out a comprehensive analysis of the evolution of stellar population properties of LRGs across cosmic time. For the first time, we derived ages, total metallicities and in particular [α/Fe] abundance ratios for a large, mass-complete sample of massive LRGs that continuously spans the redshift range $0.15 < z < 0.8$. We then investigated how their stellar population properties evolve across the last ~ 7 Gyr of the cosmic time. The continuous redshift coverage of the joined BOSS and DESI sample represents a key advancement, enabling us to probe the evolutionary trends of massive quiescent galaxies in a homogeneous and consistent way throughout this wide redshift range.

This paper is structured as follows: in Section 2 we present the selected LRG data used in our analysis and describe the treatment of the spectra to obtain high-quality stacked spectra suitable for our study. In Section 3 we describe in detail the procedures adopted to retrieve the stellar population parameters of our selected sample. In Section 4 we present the results that we obtained and the discussion of our analysis. Throughout the paper, we adopt a standard ΛCDM cosmology with $\Omega_M = 0.3089$, $\Omega_\Lambda = 0.6911$, and $H_0 = 67.8$ km s^{-1} Mpc^{-1} (Planck Collaboration 2016). Magnitudes are in the AB system (J. B. Oke 1974).

2 DATA AND SAMPLE SELECTION

In this section we present the LRG samples drawn from the DESI and BOSS surveys and their most important properties, including the stellar mass completeness limits and redshift distributions.

2.1 DESI

We used the DESI Data Release 1 (DR1; DESI Collaboration 2025), which provides all the data acquired during the first 13 months of the DESI main survey. The DESI DR1 includes spectra for more than 18 million unique targets, covering around 9500 deg^2. Although the DESI LRG survey will be completed at the end of the full observational campaign, the DR1 offers a representative and statistically significant data set of the final sample. The DESI observations have a spectral resolution of R = 2000−5000 and cover the observed wavelength range 3600−9800 Å. We selected LRGs within two mass bins [$11.3 < \log(M_*/\mathrm{M}_\odot) < 11.5$, $\log(M_*/\mathrm{M}_\odot) > 11.5$], for which completeness is ~ 80 per cent and ~ 90 per cent, respectively (R. Zhou et al. 2020, 2023). With this selection, we obtained 300 019 galaxies in the lower mass bin and 100 952 for the higher one. We limited our selection to the redshift range $0.4 < z < 0.8$, which ensures that all spectral indices used in our analysis (see Section 3.2.2) are consistently available across the full sample.

2.2 BOSS

With the aim of extending the redshift range of our study, we complement the DESI data set with the LRG sample from the BOSS survey (D. J. Eisenstein et al. 2011; K. S. Dawson et al. 2013), whose selection is focused on the redshift range $0.15 < z < 0.6$. The BOSS observations have a spectral resolution of R = 1500−2500 and cover the observed wavelength range 3600−10400 Å. The BOSS LRG sample consists of two subsamples: a low-redshift sample (LOWZ), which contains galaxies up to $z \approx 0.4$, and a high-redshift sample (CMASS) for galaxies at $z > 0.4$. According to A. Leauthaud et al. (2016), the LOWZ selection is 80 per cent complete for LRGs with $\log(M_*/\mathrm{M}_\odot) > 11.6$ in the redshift range $0.15 < z < 0.43$, while the CMASS sample is 80 per cent complete only in the narrow redshift slice $0.51 < z < 0.61$ for the same mass range. We therefore consider only the LOWZ selection, considering a single mass bin [$\log(M_*/\mathrm{M}_\odot) >$

Downloaded from academic.oup.com/mnras/article/548/4/stag766/8661535 by guest on 26 November 2026

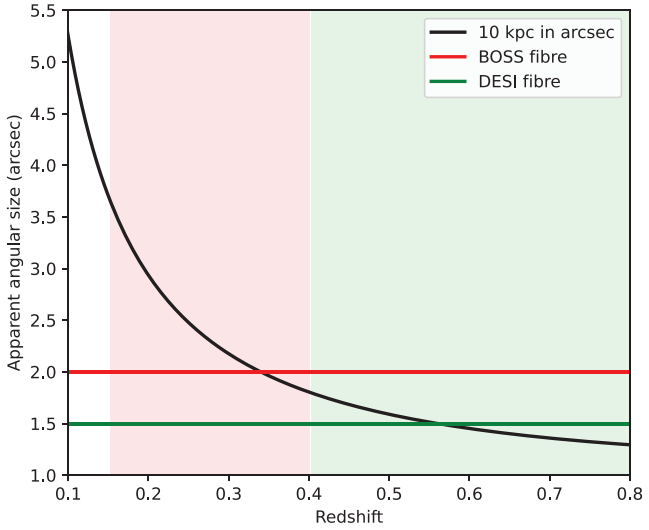


Figure 1. Apparent angular size (in arcsec) of a typical massive quiescent galaxy with a physical effective diameter of 10 kpc ($R_{eff} = 5$ kpc) as a function of redshift. The horizontal red (green) line indicates the BOSS (DESI) fibre aperture. The shaded red (green) area marks the redshift range considered for the BOSS (DESI) sample.

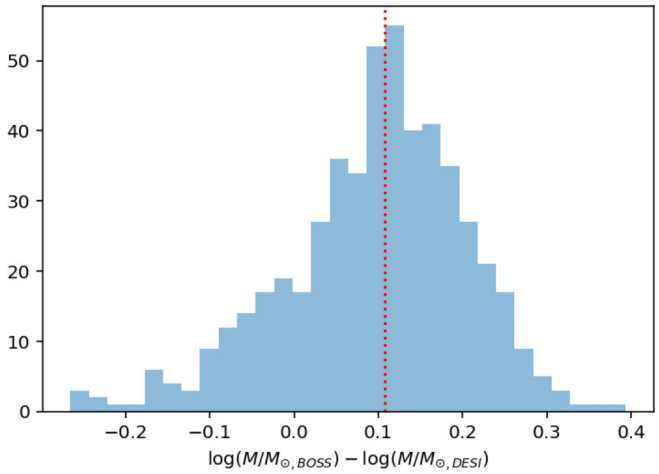


Figure 2. Histogram of the stellar mass differences for the matched galaxies in DESI and BOSS at $0.15 < z < 0.4$. The dotted line marks the median value of the distribution.

11.6] in the redshift range $0.15 < z < 0.4$ (obtaining 9528 galaxies), to ensure a fair comparison with the complete DESI sample and to study the evolutionary trends from $z = 0.8$ down to $z = 0.15$. The LRG observations in both DESI and BOSS are tuned such that the comoving number density of the observed galaxies remains approximately constant across their redshift range. This ensures that the $\sim 10-20$ per cent of galaxies not included in the final spectroscopic catalogue are missing due to a random sampling from the complete parent photometric catalogue. Therefore, our final sample is expected to be representative of the massive quiescent population. In addition, we selected LRGs in the redshift range $0.35 < z < 0.6$ as a comparison sample of galaxies observed in both in DESI and BOSS surveys, in order to assess the consistency of these two data sets (Appendix A). The results obtained from measuring the physical parameters of the same galaxies using DESI and BOSS data are perfectly matched within 1σ, reinforcing the conclusions that we have selected a representative sample of the most massive quiescent galaxies from $z = 0.8$ down to 0.15. Moreover, thanks to the uniform analysis in terms of both the techniques applied and the indices used, the conclusions are further strengthened. Details of this comparison can be found in Appendix A.

When comparing BOSS and DESI data, aperture effects must be considered, as the two surveys employ fibres of different sizes. The DESI fibre has a diameter of 1.5 arcsec, while the BOSS fibre is slightly larger, with a 2 arcsec diameter. As shown in Fig. 1, the DESI and BOSS fibre apertures correspond to roughly one effective radius (~ 5 kpc) for a typical massive quiescent galaxy (see G. Favole et al. 2018). Only at $z < 0.3$ the fraction of the galaxy included within the BOSS fibre becomes significantly smaller than one R_e. Consequently, considering possible and likely stellar population gradients, the results at very low redshift may not be easily comparable to those at higher redshift. We will take into account this difference when comparing the derived physical properties of the stellar content of galaxies at low redshift.

We investigated potential differences of the stellar mass estimates between the DESI and BOSS surveys, by selecting LRGs observed in both, at $0.15 < z < 0.4$, and applying the DESI mass threshold used for the sample comparison ($\log(M_*/M_{\odot,DESI}) > 11.5$), for which we obtained 517 matched galaxies. Stellar masses in the BOSS sample were derived assuming a Kroupa IMF (see C. Maraston et al. 2013), while DESI masses were estimated assuming a Chabrier IMF. In addition, the two surveys rely on different photometric data and spectral energy distribution (SED) fitting procedures. Fig. 2 shows the stellar mass differences for the matched galaxies in DESI and BOSS. We found a median offset of ~ 0.1 dex, fully consistent with expected IMF-driven difference between Kroupa and Chabrier IMF assumptions (~ 0.05 dex, e.g. M. Longhetti & P. Saracco 2009; M. Bernardi et al. 2010) and different templates assumptions in the SED fitting procedures. We verified this by applying the median offset described above to the BOSS stellar masses of the main sample, and after this correction the two distributions, along with their median values ($\log(M_*/M_{\odot,DESI}) = 11.57$, $\log(M_*/M_{\odot,BOSS}) = 11.56$), are fully consistent, showing consistent shapes. Given that the uncertainties associated with the stellar mass estimates derived from SED fitting (i.e. $0.1 - 0.5$ dex) closely match the observed spread in mass differences between BOSS and DESI for the same galaxies, we can safely conclude that no systematic bias is introduced in the mass sample selection from the two surveys. Therefore, since DESI masses are smaller by ~ 0.1 dex than the BOSS ones, the $\log(M_*/M_{\odot}) > 11.5$ DESI sample corresponds to the selection of BOSS galaxies with $\log(M_*/M_{\odot}) > 11.6$.

2.3 Further spectroscopic selection

Although the LRG samples are dominated by quiescent galaxies, their selection on a purely photometric basis means that a fraction of emission-line galaxies is inevitably included. Indeed, from the DR1/Iron value-added catalogue (DESI Collaboration 2025) and from the EmissionLinesPort table of the SDSS data base (C. Maraston et al. 2013), we find that the spectra of the initially selected galaxies still show some emission features, detected even at the low signal-to-noise (S/N) ratio of the two sets of data. To obtain a clean sample of quiescent galaxies, whose absorption lines are unaffected, or only minimally affected, by ongoing star formation or nuclear activity, we applied an additional selection criterion. We use the following spectroscopic in-

Downloaded from academic.oup.com/mnras/article/548/4/stag766/8661535 by guest on 26 November 2026

Table 1. Number of galaxies in the BOSS and DESI samples after all the selection cuts applied in this work.

	BOSS sample	DESI sample
LRG selection	9528	400 971
Emission lines cut	6160	224 589
Post-starburst cut	5954	194 419

dicators: $[\mathrm{O\,II}]_{\lambda3727}$, H$\delta$, H$\beta$, and $[\mathrm{O\,III}]_{\lambda5007}$, to define a subsample of spectroscopically confirmed quiescent galaxies satisfying these criteria:

(i) EW($[\mathrm{O\,III}]_{\lambda5007}$) < 1 Å;
(ii) EW(Hβ) < 1 Å;
(iii) EW($[\mathrm{O\,II}]_{\lambda3727}$) < 5 Å;
(iv) EW(Hδ) < 1 Å.

Here EW stands for equivalent width defined such that positive values correspond to emission. These criteria are designed to select galaxies with no detectable $[\mathrm{O\,III}]_{\lambda5007}$, H$\beta$, and H$\delta$ emission lines and at most a weak $[\mathrm{O\,II}]_{\lambda3727}$ emission (considering the blended spectral line), which can occur in quiescent galaxies at these redshifts (see M. V. Maseda et al. 2021; F. R. Ditrani et al. 2025). We took the values of the EW of the considered emission lines from the previously cited data bases, i.e. the DR1/Iron value-added catalogue for the DESI sample, and the emissionLinePort table for the BOSS sample. Using the criteria described above, we obtained 224 589 galaxies from the DESI survey (170 901 in the lower mass bin, 53 688 in the higher one), and 6160 galaxies for the BOSS one. Finally, we added a last criterion, EW(Hδ) > -3 Å, to exclude post-starburst galaxies from our sample, following the definition of B. M. Poggianti et al. (2009) and A. Werle et al. (2022). Galaxies with stronger Hδ in absorption are recently quenched galaxies, which are likely to have experienced a different evolutionary track compared to the older quiescent galaxies that compose our sample. The final sample contains 194 419 quiescent galaxies from the DESI survey (149 243 in the lower mass bin, 45 176 in the higher one), and 5954 from the BOSS selection. Table 1 summarizes the selected galaxies after each selection cut.

2.4 Stacked spectra

The BOSS and DESI samples provide us with a rich statistical sample of LRGs, albeit at a median S/N per Å insufficient to robustly determine the stellar population parameters of the selected population on individual spectra. We therefore stack blocks of individual spectra to boost the S/N in order to reach an S/N of ~ 20/Å in the rest-frame range 4000−4200 Å. In the DESI sample, at $0.4 < z < 0.8$, the median S/N of individual spectra in the considered wavelength range is around 4/Å. Therefore, we stacked the individual spectra in groups of 50 objects, in bins of $\Delta z = 0.01$, within two mass bins [$11.3 < \log(M_*/\mathrm{M}_\odot) < 11.5$, $\log(M_*/\mathrm{M}_\odot) > 11.5$], in order to stack galaxies with similar properties in the $z-\log(M_*/\mathrm{M}_\odot)$ plane. We did not homogenized in a velocity dispersion prior to stacking for two main reasons. First, due to the low S/N of individual spectra, the single galaxy measurements of velocity dispersion carry significant uncertainties, and a deconvolution or broadening to a common scale could introduce more noise. Second, our sample is strictly limited to the most massive quiescent galaxies ($\log(M_*/\mathrm{M}_\odot) > 11.3$). At these high masses, the galaxies naturally reside in a regime of high and relatively uniform velocity dispersion. We therefore rely on the homogeneity of our stellar mass selection to ensure that the stacked features are not artificially diluted. We shifted the individual spectra to their rest-frame, and we normalized their flux within 5150−5500 Å. The chosen stacking redshift bin is wide enough to include spectra with slightly different observed wavelength ranges, allowing for optimal removal of bad pixels and sky-subtraction residuals. For each stacked spectrum, we generated 201 bootstrap realizations by randomly resampling, with replacement, the set of 50 spectra in each bin. In each realization, 50 spectra were drawn, allowing individual spectra to appear multiple times, and co-added following the same procedure adopted for the original stack. The dispersion among the resulting stacks was then used to estimate robust pixel-by-pixel uncertainties. From this step we obtained 2835 stacked spectra in the mass bin $11.3 < \log(M_*/\mathrm{M}_\odot) < 11.5$ and 842 in the mass bin $\log(M_*/\mathrm{M}_\odot) > 11.5$.

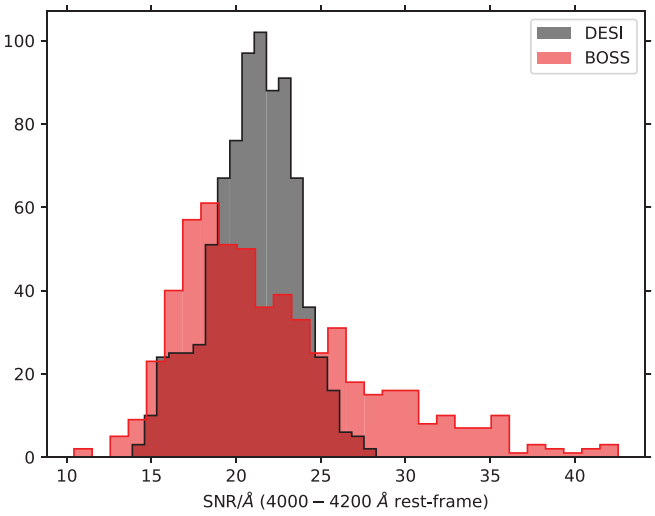


Figure 3. S/N distributions for the DESI stacked spectra, in black, and BOSS, in red, in the rest-frame range 4000 − 4200 Å.

Regarding the BOSS sample, the median S/N of individual spectra is around 8/Å in the rest-frame range 4000−4200 Å, therefore we stacked groups of 10 spectra in order to achieve an S/N comparable to that of the DESI stacked spectra. From this step we obtained 581 BOSS stacked spectra. Fig. 3 shows the S/N distributions for the DESI and BOSS stacked spectra in the rest-frame range 4000−4200 Å. The BOSS distribution shows a more extended high-S/N tail than DESI, indicating a larger fraction of spectra at high S/N, while the median values are consistent to S/N ~ 21.5/Å. The choice of the number of spectra to be stacked ensures reliable measurements of the stellar population properties and their intrinsic spread across the redshift range by stacking only the minimum number of spectra required. This approach preserves sensitivity to the intrinsic variation within the sample, which would otherwise be lost if all available spectra were combined into a single very high-S/N stack.

3 ANALYSIS

Our goal is to characterize the star formation and chemical enrichment history of the most massive quiescent galaxies through their light-weighted age, stellar metallicity, and [α/Fe] abundance. In this section, we describe in detail the steps of the analysis performed on our sample. Specifically, in Section 3.1 we introduce the two stellar population models used to analyse the

Downloaded from academic.oup.com/mnras/article/548/4/stag766/8661535 by guest on 26 November 2026

selected galaxies. In Sections 3.2 and 3.3 we describe in detail how we obtained the estimate of stellar kinematics, the extraction of the stellar components and the measurements of the stellar population parameters using Monte Carlo techniques. Finally we present how we assess the stellar population parameters as a function of redshift using the hierarchical Bayesian modelling (Section 3.4).

3.1 Stellar population models

We used two spectrophotometric models to measure the light-weighted age, stellar metallicity and [α/Fe] from the stacked spectra. The first set corresponds to the semi-empirical simple stellar populations (SSPs) models from A. T. Knowles et al. (2023) (sMILES hereafter). These SSP models adopt the BaSTI evolutionary tracks (A. Pietrinferni et al. 2004, 2006) and the MILES empirical stellar library (3540.5 $< \lambda <$ 7350.2 Å; P. Sánchez-Blázquez et al. 2006; J. Falcón-Barroso et al. 2011, 2.5 Å FWHM resolution). We assumed a Kroupa IMF (P. Kroupa 2001). The synthetic library provides 2650 SSPs unevenly spaced in linear age and [M/H], covering 53 ages from 0.03 Gyr to 14 Gyr, 10 metallicities from [M/H] $= -1.79$ to [M/H] $= 0.26$ dex, the solar abundance $Z_\odot = 0.0198$, and 5 [α/Fe] abundances from -0.2 to 0.6 dex. The second set is that of D. Thomas, C. Maraston & J. Johansson (2011) (hereafter TMJ). These models are based on the Cassisi evolutionary tracks (S. Cassisi, M. Castellani & V. Castellani 1997), the MILES empirical stellar library, and assume a Kroupa IMF. For these models, the synthetic library provides predictions of 25 Lick indices for each SSP (G. Worthey et al. 1994). The SSPs are unevenly spaced in linear age and [M/H], covering 20 ages from 0.1 Gyr to 15 Gyr, 6 metallicities from [M/H] $= -2.25$ to [M/H] $= 0.67$ dex (with solar abundance $Z_\odot = 0.02$), and 5 [α/Fe] abundance ratios from -0.3 to 0.5 dex.

In the following, we use these two stellar population models to perform parallel analyses of our sample, allowing us to compare the derived stellar population parameters under different modelling assumptions. We present the details of the methodology and results obtained with each model in the subsequent sections.

3.2 sMILES analysis

3.2.1 Kinematics and residual emission lines subtraction

For each stacked spectrum in the sample, we derived the kinematic parameters (i.e. recession velocity residuals and velocity dispersion) using the latest version of the pPXF code[1](M. Cappellari & E. Emsellem 2004; M. Cappellari 2023). We adopted stellar templates from the MILES stellar spectral library and performed the fit over the rest-frame wavelength range 3800−5500 Å. The synthetic templates were shifted to match each galaxy's residual recession velocity and convolved with the corresponding stellar velocity dispersion. We masked the Balmer line regions to avoid that possible small residuals of emission lines affect the fit of the continuum. Although we applied the spectroscopic criteria outlined in Section 2 to select our sample galaxies, since the individual spectra have low S/N, they might be affected by weak nebular emission filling in the cores of absorption features. To mitigate this effect, we analysed the stacked spectra for the presence of residual nebular emission in the Balmer lines. Thanks to their high S/N ratio, even small emission-line contributions can be reliably identified and assessed. This is especially important for the $H\beta$ region, where even modest emission can bias the inferred stellar ages. We therefore performed an additional two-step pPXF spectral fitting to extract the nebular emission component from each stacked spectrum, fixing the kinematics to the results obtained in the first stage. In the first step, we fitted only Hβ emission line within the wavelength range 4000 Å $< \lambda <$ 5500 Å, to obtain a reliable estimate of the nebular kinematics. In the second step, using the same wavelength range, we simultaneously fitted $H\delta$, $H\gamma$ and $H\beta$ emission lines while keeping the nebular kinematics fixed to the values obtained in the first step. We retained only those fits for which the recovered Balmer fluxes follow the expected sequence $H\delta < H\gamma < H\beta$. For the rare cases (i.e. about 15 per cent of the stacked spectra) in which a very weak Hβ line is detected and, due to the extreme weakness of the higher order Balmer lines, their flux cannot be reliably estimated by directly fitting the spectrum, we assumed the case-B Balmer line ratios to avoid unphysical solutions (D. E. Osterbrock 1989). Finally, we subtracted the best-fitting nebular component from the global spectrum, yielding a clean stellar component spectrum. We then performed 1000 realizations of the nebular best-fit by perturbing the emission line fluxes according to their associated flux uncertainties, in order to estimate the pixel-wise errors in the $H\delta$, $H\gamma$, and $H\beta$ regions of the nebular component. These estimated uncertainties were then added in quadrature to those of the stacked spectrum.

3.2.2 Full-index fitting

We adopted the full-index fitting approach (FIF; I. Martín-Navarro et al. 2015; F. R. Ditrani et al. 2025) to compare the observed spectra with the synthetic spectral templates. Unlike the more classic index fitting approach, FIF compares the flux within a specific absorption feature (with respect to its continuum value) pixel by pixel rather than averaging it. This pixel-level comparison within the index window is more effective in breaking the degeneracy between age and metallicity compared to the classical index analysis, as it accounts not only for the strength of the absorption feature but also for its detailed shape, which provides additional information about the stellar population parameters. (I. Martín-Navarro et al. 2019; F. R. Ditrani et al. 2024). We applied the FIF method to a comprehensive set of spectral indices sensitive to the age, stellar metallicity and [α/Fe], listed in Table 2. Because our fitting scheme includes Balmer lines together with Fe- and Mg-sensitive indices, the inferred [α/Fe] ratio effectively traces the [Mg/Fe] abundance ratio. Magnesium is the only α-element directly constrained by our index set, whereas the remaining α-elements (e.g. O, Si, Ca, Ti) have negligible effects on the indices used. As a consequence, the [α/Fe] values returned by the models should be interpreted as [Mg/Fe] proxy rather than as fully general α-enhancement measurements. Moreover, since we are fitting spectra with a single SSP, the derived age corresponds to the SSP-equivalent age, i.e. the age of the SSP that best reproduces the observed spectrum. In practice, this quantity closely traces the light-weighted age, since the fit is driven by the luminosity-weighted contribution of the underlying stellar populations. Therefore we define the age measurements in this work as the light-weighted age of the stellar populations. Fig. 4 shows an example of the FIF approach applied to one of the DESI stacked spectra. The best-fitting template closely matches

[1]https://pypi.org/project/ppxf/

Downloaded from academic.oup.com/mnras/article/548/4/stag766/8661535 by guest on 26 November 2026

Table 2. Spectral indices used for our analysis.

Index	Blue pseudocontinuum	Central feature	Red pseudocontinuum	$\text{Fit}_{\text{sMILES}}$	Fit_{TMJ}	Ref.
$H\delta_F$	4057.25–4088.50	4091.00–4112.25	4114.75–4137.25	$[\alpha/\text{Fe}] = 0$	Variable $[\alpha/\text{Fe}]$	1
$H\gamma_F$	4283.50–4319.75	4331.25–4352.25	4354.75–4384.75	$[\alpha/\text{Fe}] = 0$	Variable $[\alpha/\text{Fe}]$	1
Fe4383	4359.125–4370.375	4369.125–4420.375	4442.875–4455.375	Variable $[\alpha/\text{Fe}]$	Variable $[\alpha/\text{Fe}]$	1
$H\beta_o$	4821.175–4838.404	4839.275–4877.097	4897.445–4915.845	$[\alpha/\text{Fe}] = 0$	Variable $[\alpha/\text{Fe}]$	2
Mgb	5142.625–5161.375	5160.125–5192.625	5191.375–5206.375	Variable $[\alpha/\text{Fe}]$	Variable $[\alpha/\text{Fe}]$	1
Fe5270	5233.150–5248.150	5245.650–5285.650	5285.650–5318.150	Variable $[\alpha/\text{Fe}]$	Variable $[\alpha/\text{Fe}]$	1
Fe5335	5304.625–5315.875	5312.125–5352.125	5353.375–5363.375	Variable $[\alpha/\text{Fe}]$	Variable $[\alpha/\text{Fe}]$	1

Note. (1) G. Worthey et al. (1994); (2) J. Cervantes & A. Vazdekis (2009).

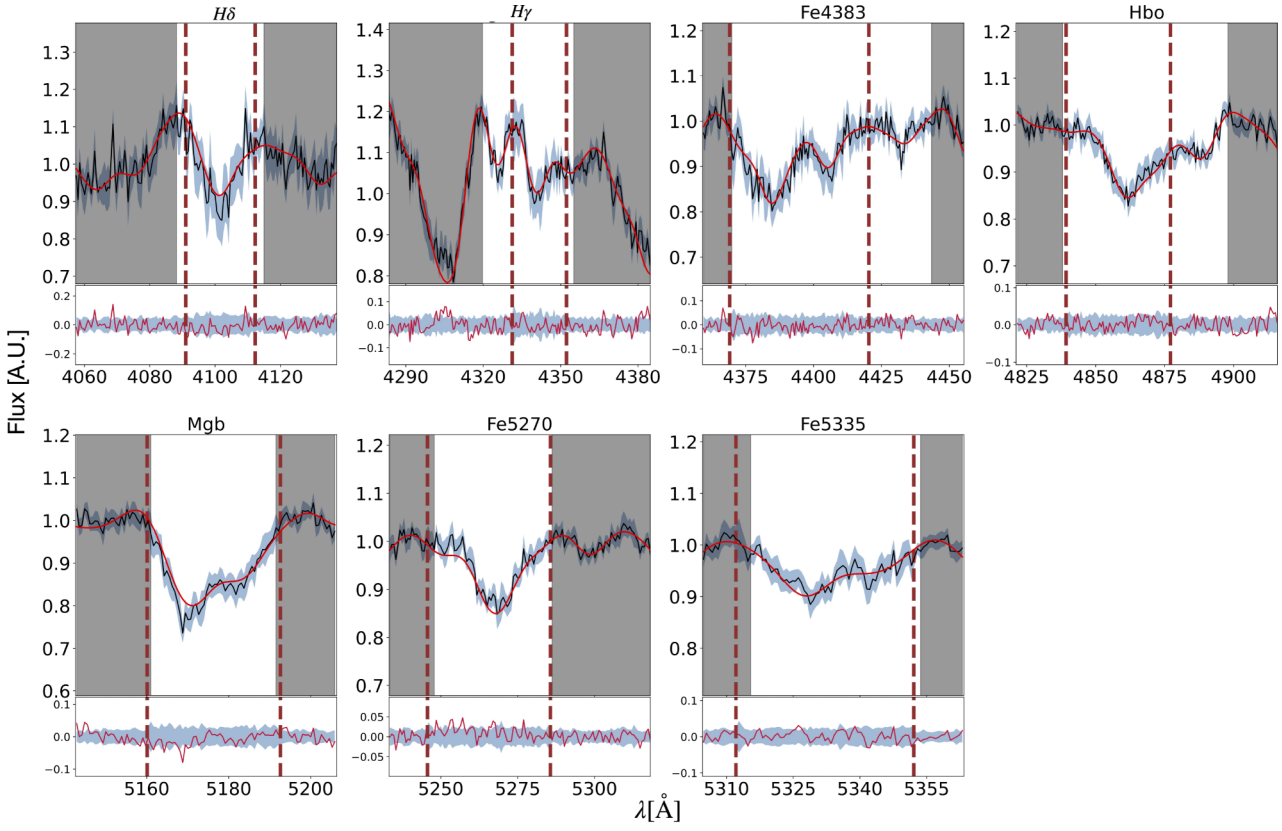


Figure 4. FIF application on the selected indices for a stacked spectrum in the DESI sample. The vertical dashed brown lines indicate the feature boundaries for each index, while the grey shaded area represents the pseudo-continua regions used for normalization. In the upper subplots, the black lines and blue shaded regions correspond to the stacked spectrum and its associated uncertainty, respectively. The solid red line represents the best-fit derived from the posterior distribution. The red lines in the lower subplots show the residuals between the observed spectrum and the best fit, with the blue shaded region indicating the relative uncertainties of the stacked spectrum.

each spectral feature, capturing detailed information from both its depth and shape.

Modelling the effect of $[\alpha/\text{Fe}] \neq 0$ (see A. Vazdekis et al. 2015; A. T. Knowles et al. 2023) models is known to be problematic, as it relies on stellar models computed under the assumption of local thermodynamic equilibrium (LTE), which may underestimate Balmer line depths in α-enhanced or hot stellar populations, where non-LTE effects are known to be non-negligible. Moreover, in practice, the effect of varying the α-elements might be balanced by variations of other elements (e.g. C). To mitigate these effects, for sMILES we fitted the set of indices $[H\delta_F, H\gamma_F, H\beta_o]$ adopting SSP templates corresponding to $[\alpha/\text{Fe}] = 0$, while we fitted the remaining indices using SSPs with variable $[\alpha/\text{Fe}]$ abundance ratio. We computed the total posterior probability distribution using the likelihood given by $\mathcal{L} = e^{-\chi^2/2}$, with

$$\chi^2 = \sum_i \left(\frac{F_{\text{obs}_i} - F_{\text{syn}_i}}{\sigma_{\text{obs}_i}} \right)^2, \quad (1)$$

where F_{syn_i} is the flux of the synthetic spectrum along the feature of each index, and F_{obs_i} is the flux of the observed spectrum with the error σ_{obs_i}. We derived posterior probability distributions and the Bayesian evidence using the nested sampling Monte Carlo algorithm MLFriends (J. Buchner 2016, 2019) using the UltraNest[2] package (J. Buchner 2021). We assumed a uniform prior for all the parameters considered, summarized in Table 3. Fig. 5 shows

[2] https://johannesbuchner.github.io/UltraNest/

Downloaded from academic.oup.com/mnras/article/548/4/stag766/8661535 by guest on 26 November 2026

Table 3. The three free parameters fitted to our spectroscopic data, along with their associated prior distributions.

Parameter	Unit	Range	Prior	Model
$\mathrm{Age_{model}}$	Gyr	$(0, \mathrm{Age_{Universe}})$	Uniform	sMILES
[M/H]	dex	$(-1.79, 0.26)$	Uniform	sMILES
[α/Fe]	dex	$(-0.2, 0.6)$	Uniform	sMILES
$\mathrm{Age_{model}}$	Gyr	$(0, \mathrm{Age_{Universe}})$	Uniform	TMJ
[M/H]	dex	$(-2.25, 0.67)$	Uniform	TMJ
[α/Fe]	dex	$(-0.3, 0.5)$	Uniform	TMJ

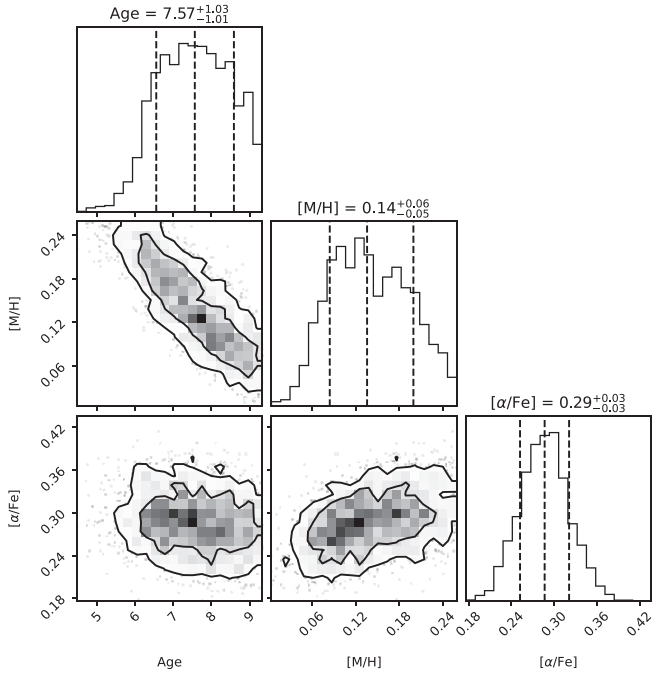


Figure 5. Example of the joint and marginal posterior distributions of light-weighted age, [M/H], and [α/Fe] for a DESI stacked spectrum at $z = 0.4$ and $\log(M_*/\mathrm{M}_\odot) = 11.6$. Contours represent the 68 per cent and 95 per cent probability levels. The 16 per cent, 50 per cent, and 84 per cent intervals are indicated as dashed lines.

an example of the joint and marginal probability distributions for all the fitted parameters.

This technique of full-index fitting combined with the nested sampling algorithm has been implemented in a PYTHON routine, named **INFUSE** [3] (Full-INdex Fitting for Uncovering Stellar Evolution), which we publicly release with this work.

3.3 TMJ analysis

The analysis based on the TMJ models follows the same general procedure adopted for the sMILES analysis, with the important distinction that TMJ provides predictions for absorption-line indices rather than synthetic spectra. Since the spectral resolution of TMJ cannot be adapted to the effective resolution of our stacked spectra, the latter must be degraded to the model resolution to ensure consistency with the model predictions. For this reason, before performing any kinematic measurement and emission-line correction, we first homogenized the stacked spectra by convolving them to the fixed spectral resolution of the TMJ models (FWHM = 2.51 Å). After that, we carried out the same procedure adopted for the sMILES analysis to measure the stellar kinematics and perform the removal of emission line residuals (see Section 3.2.1).

Since the TMJ models provide predictions for absorption-line indices, we carried out the stellar population analysis using the classical index-strength approach. For consistency with the sMILES analysis, we measured the same set of indices listed in Table 2 on each stacked spectrum. In this analysis we considered the effect of [α/Fe] also on higher-order Balmer lines (see Table 2), for which the TMJ models provide a robust calibration (D. Thomas, C. Maraston & A. Korn 2004). Because the observed spectra are broadened by the stellar velocity dispersion, we corrected the measured indices for this effect following the procedure described in D. Thomas et al. (2010) (see also H. Kuntschner 2004). We derived the correction factor using the best-fitting pPXF template obtained for each stacked spectrum, as follows: first, we measure each index on the best-fitting template spectrum degraded only to the TMJ spectral resolution (FWHM = 2.51 Å) and with zero velocity dispersion; second, convolve the same best-fitting template with the stellar velocity dispersion obtained from pPXF fit, and measure the indices again. The ratio:

$$C = \frac{I_{\mathrm{bestfit}}}{I_{\mathrm{bestfit,\ broadened}}} \tag{2}$$

provides the multiplicative correction factor applied to the observed indices. This procedure ensures that the observed line strengths are brought onto the TMJ index system at fixed resolution and zero velocity dispersion, allowing a direct comparison with the model predictions. Fig. 6 shows the Balmer line indices $\mathrm{H}\delta_F$, $\mathrm{H}\gamma_F$, and $\mathrm{H}\beta$ as functions of Mgb and Fe5270 for TMJ models, together with the corresponding indices measured on the DESI stacked spectra as a function of the redshift. The comparison clearly illustrates that the models span the region occupied by the data, and highlights the important role that abundance ratios might have in interpreting these spectral indices.

We computed the total posterior probability distribution using the likelihood given by $\mathcal{L} = e^{-\chi^2/2}$, with:

$$\chi^2 = \sum_i \left(\frac{I_{\mathrm{obs}_i} - I_{\mathrm{syn}_i}}{\sigma_{\mathrm{obs}_i}} \right)^2, \tag{3}$$

where I_{obs_i} is the ith spectral index measured in the stacked spectrum, I_{syn_i} is the index prediction of the models, and σ_{obs_i} is the observational error of the ith spectral index. The observational errors have been evaluated as the standard deviation of the distribution of 1000 random Gaussian realizations of the perturbed stacked spectrum. We derived posterior probability distributions using the UltraNest algorithm, assuming a uniform prior for all the parameters considered, summarized in Table 3.

3.4 Hierarchical Bayesian modelling

To assess the stellar population parameters as a function of redshift, we grouped the stacked spectra into redshift bins. We adopted bins of width $\Delta z = 0.05$, and for each bin we used the corresponding stacked spectra falling within that redshift interval, to ensure to have a statistically significant sample in each bin. We then combined the posteriors of each stacked spectrum using the hierarchical Bayesian modelling. In the hierarchical framework, our models consist of two levels: the first level involves

[3] https://infuse-fit.readthedocs.io/en/latest/

Downloaded from academic.oup.com/mnras/article/548/4/stag766/8661535 by guest on 26 November 2026

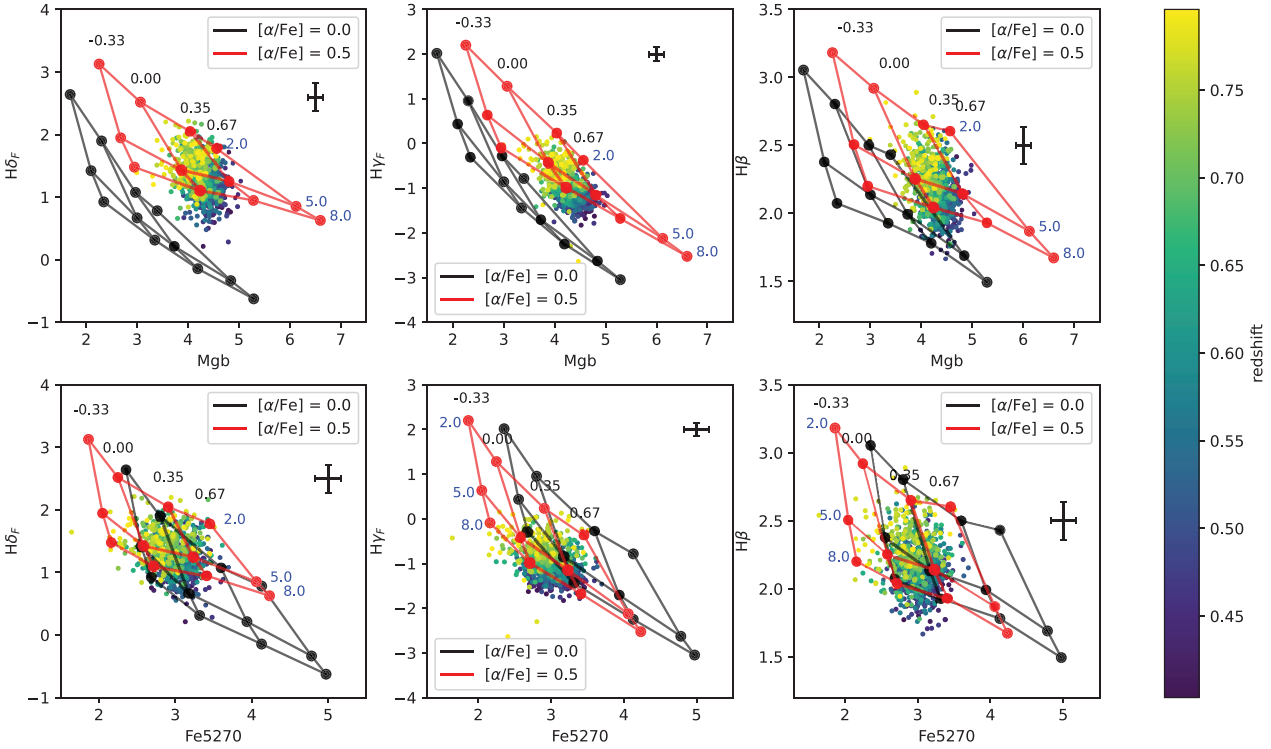


Figure 6. Balmer line indices Hδ_F, Hγ_F, and Hβ as functions of Mgb (top panels) and Fe5270 bottom panels. Red and black lines are the α/Fe-enhanced and the solar-scale values for the TMJ models, respectively. Models for the ages 2, 5, and 8 Gyr, and the metallicities [M/H] $= -0.33$, 0.0, 0.35, and 0.67 dex are shown. The circles mark the measured indices on the DESI stacked spectra, colour-coded as a function of the redshift. The error bars denote average 1σ errors.

the measurements of the parameters for each individual stacked spectrum, while the second level describes how the measurements are distributed within each redshift bin. Differently from the classic stacked spectra fit, this approach has several advantages as it avoids introducing correlated noise caused by smoothing the individual spectra to a common velocity dispersion and by the continuum interpolation with polynomials (see appendix B in A. G. Beverage et al. 2023). Following the'a posteriori' approach (e.g. A. G. Beverage et al. 2023; F. R. Ditrani et al. 2025), as the first level of the models we computed the posterior probability distribution of each physical parameter listed in Table 3 for each individual stacked spectrum as detailed in Sections 3.2.2 and 3.3. Then, as a second level of modelling, we fitted the distribution of the posteriors of each parameter with a Gaussian function plus an outlier model in each redshift bin. This approach provides a mean value for each parameter in each selected redshift bin, the intrinsic scatter of our sample, along with a reliable estimate of the uncertainties. The measurement of each parameter is then treated independently in each redshift bin, with no assumption on the redshift evolution of the stellar population parameters. We assumed the same prior listed in Table 3 for each parameter, then we applied a logarithmically uniform prior for the intrinsic scatter between 0.01 and 10 dex, and a uniform prior for the fraction of outliers within 0−20 per cent. Fig. 7 shows an example of the posterior probability distribution of the [M/H] parameter, its scatter, and the fraction of outliers for the DESI spectra in the redshift bin $0.45 < z < 0.5$ and mass bin [$\log(M_*/M_\odot) > 11.5$]).

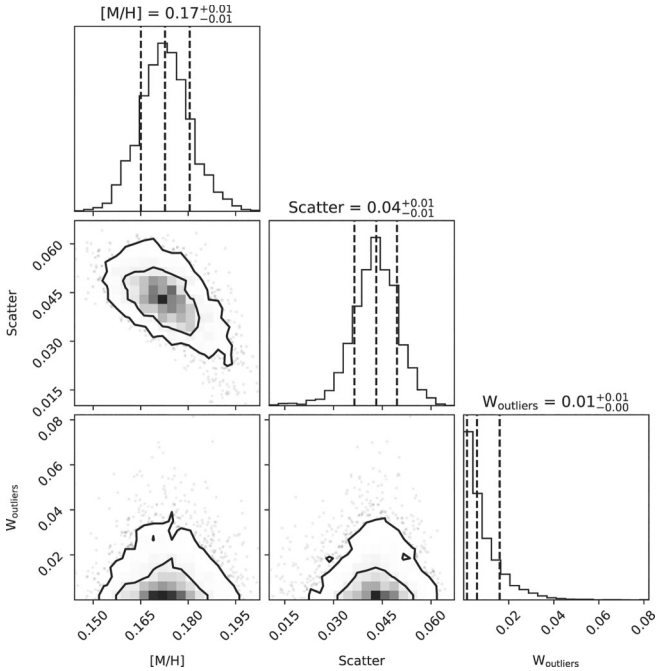


Figure 7. Corner plot summary of the posterior distributions of the [M/H], its scatter, and the fraction of outliers obtained for all the stacked spectra contained in the redshift range $0.45 < z < 0.5$ and [$\log(M_*/M_\odot) > 11.5$] bin. Contours are at the 68 per cent and 95 per cent probability. The 16 per cent, 50 per cent and 84 per cent intervals are indicated by dashed lines.

Downloaded from academic.oup.com/mnras/article/548/4/stag766/8661535 by guest on 26 November 2026

4 RESULTS

In the following we present the results obtained using both the sMILES and TMJ models. Specifically, we discuss the stellar population parameters of the DESI stacked spectra in two distinct mass bins, and the redshift evolution of these parameters of the most massive galaxies across the full BOSS and DESI redshift range.

When comparing stellar population parameters derived using the TMJ and sMILES models, one should be aware of an important difference. Both frameworks provide a total metallicity [M/H], but the resulting values are not directly comparable, as each assumes a different α-elements mixture at fixed iron abundance. In practice, while Fe and Mg are the only elements directly and robustly constrained by the spectral indices used in this work, the remaining metal content is model dependent and inferred through the adopted α-element pattern. Indeed, in the sMILES models the [α/Fe] ratio accounts for variations in the α-elements O, Ne, S, Mg, Si, Ca, and Ti. In contrast, in the TMJ models the definition of the α-enhanced mixture additionally includes C, N, and Na, whose abundances are modified alongside the other α-elements. The relation between [Fe/H], [α/Fe] and [M/H] differs substantially between the two sets of models:

$$[\mathrm{M/H}]_{\mathrm{sMILES}} = [\mathrm{Fe/H}] + 0.66\,[\alpha/\mathrm{Fe}] + 0.20\,[\alpha/\mathrm{Fe}]^2 \quad (4)$$

$$[\mathrm{M/H}]_{\mathrm{TMJ}} = [\mathrm{Fe/H}] + 0.94\,[\alpha/\mathrm{Fe}]\,. \quad (5)$$

As a consequence, the [M/H] parameter directly returned by the fit cannot be compared at face value. In contrast, [Fe/H] is the most robust quantity to compare between the two models, because it is directly constrained by Fe-sensitive spectral lines and is only weakly affected by model-dependent assumptions about α-element enhancement. For this reason, in the following we compare light-weighted age, and separately [Fe/H], and [α/Fe] between TMJ and sMILES, since [M/H] is a different combination of the two quantities above for the two models.

Fig. 8 shows the evolution of the light-weighted age, [Fe/H] and [α/Fe] in the redshift range $0.4 < z < 0.8$ for the DESI sample in the two mass bins [$11.3 < \log(M_*/\mathrm{M}_\odot) < 11.5$, and $\log(M_*/\mathrm{M}_\odot) > 11.5$]. As described in Section 3.4, we estimated the mean and intrinsic scatter of each parameter in redshift bins of width $\Delta z = 0.05$. The distributions of the stellar population parameters follow consistent trends across the entire redshift range for the two mass bins, suggesting similar star formation histories. These trends are also consistent across the sMILES and TMJ models, with the most significant differences found in the light-weighted age and [α/Fe] values. Within each redshift bin, we found no evidence for significant intrinsic scatter beyond the observational uncertainties of the individual stacked spectra, suggesting that the galaxy population is nearly homogeneous. Overall, galaxies in the higher mass bin exhibit systematically older ages and higher [α/Fe] across the entire redshift range covered by DESI, while [Fe/H] is consistent in the two mass bins, although these differences remain within the 1σ uncertainties.

Fig. 9 shows the evolution of the light-weighted age, [Fe/H] and [α/Fe] in the redshift range $0.15 < z < 0.8$ of stacked spectra of galaxies of the BOSS and DESI samples, for the common mass bin [$\log(M_*/\mathrm{M}_\odot) > 11.5$]. Also in this case, we estimated the mean and intrinsic scatter of each parameter in redshift bins of width $\Delta z = 0.05$. Overall, the two surveys show consistent evolutionary trends and all parameters exhibit clear correlations with redshift. Despite being independent data sets, the BOSS and DESI results agree well in the redshift range where they overlap, supporting a consistent selection function of LRGs and similar mass estimates in both surveys (as compared in Section 2). For both the BOSS and DESI results we found no evidence for significant intrinsic scatter beyond the observational uncertainties of the individual stacked spectra. In both samples, galaxies exhibit an evolution of the light-weighted age consistent with a pure passive evolution, with a nearly constant offset between the age of the Universe and the measured stellar ages. The galaxies' [Fe/H] and [α/Fe] show an overall flat trend towards lower redshift. These trends are recovered using both the sMILES and TMJ models, even if the two analyses yield different absolute values for [Fe/H] and [α/Fe]. In particular, the sMILES models return systematically higher [Fe/H] and lower [α/Fe] compared to TMJ, while preserving the same redshift dependence. The systematic differences in [α/Fe] and [Fe/H] between the results using the two models are mainly driven by their different definitions of the α-elements mixture. As described before, the TMJ models, in their definition of [α/Fe], follow a lockstep enrichment pattern where C and N are increased alongside the traditional α-elements. In contrast the sMILES models vary in lockstep only the traditional α-elements. The TMJ models' consideration of a larger number of enhanced elements explains the constant offset we observe. Indeed TMJ yields consistently higher [α/Fe] to match the same absorption features. This modelling choice indirectly impacts the inferred iron abundance as well, in which we observe slightly lower [Fe/H] with TMJ models with respect to the sMILES results.

5 MOST MASSIVE QUIESCENT GALAXIES IN THE ILLUSTRISTNG SIMULATION

The IllustrisTNG simulations (A. Pillepich et al. 2018; V. Springel et al. 2018; D. Nelson et al. 2019, TNG hereafter) are a series of cosmological gravity+magnetohydrodynamical simulations that model a range of physical processes for the formation of galaxies. Each TNG simulation includes a comprehensive model of galaxy formation and evolution from $z = 127$ to $z = 0$, generating several snapshots across the cosmic time. The initial conditions of the TNG snapshots have been initialized at $z = 127$ assuming a matter density $\Omega_m = \Omega_{dm} + \Omega_b = 0.3089$, baryonic density $\Omega_b = 0.0486$, cosmological constant $\Omega_\Lambda = 0.6911$, Hubble constant $H_0 = 100h$ km s^{-1} Mpc^{-1} with $h = 0.6774$ (Planck Collaboration 2016). In this work, we considered the largest TNG box: TNG300-1, which has a side length of 300 Mpc. For our analysis, we considered snapshots within the redshift range $0.15 < z < 0.8$, in order to compare the stellar population parameters of simulated galaxies with those obtained from the spectral analysis of our sample. Specifically, we used the full output snapshots at $z = [0.7, 0.5, 0.4, 0.3, 0.2]$, as the [$\alpha$/Fe] information is only available in the full snapshots. For each snapshot, we selected galaxies with $\log(M_*/\mathrm{M}_\odot) > 11.5$ and $\log(\mathrm{sSFR}) < -11$, following selection criteria consistent with those we adopted for the BOSS and DESI samples. Moreover, we derived light-weighted age, [Fe/H] and [α/Fe] within one effective radius of each galaxy, to ensure consistency between simulated and observed values. The sMILES and TMJ models consider different elements in the definition of [α/Fe], therefore we derived two estimates from the TNG element abundances. Indeed, the simulation provides individual abundances for H, He, C, N, O, Ne, Mg, Si, and Fe, but not for S, Ca, or Ti. However, the absence of these elements has a negligible impact on our analysis, as the dominant contribution to the total metal budget comes from O, C, N, and Mg (see F. La Barbera et

Downloaded from academic.oup.com/mnras/article/548/4/stag766/8661535 by guest on 26 November 2026

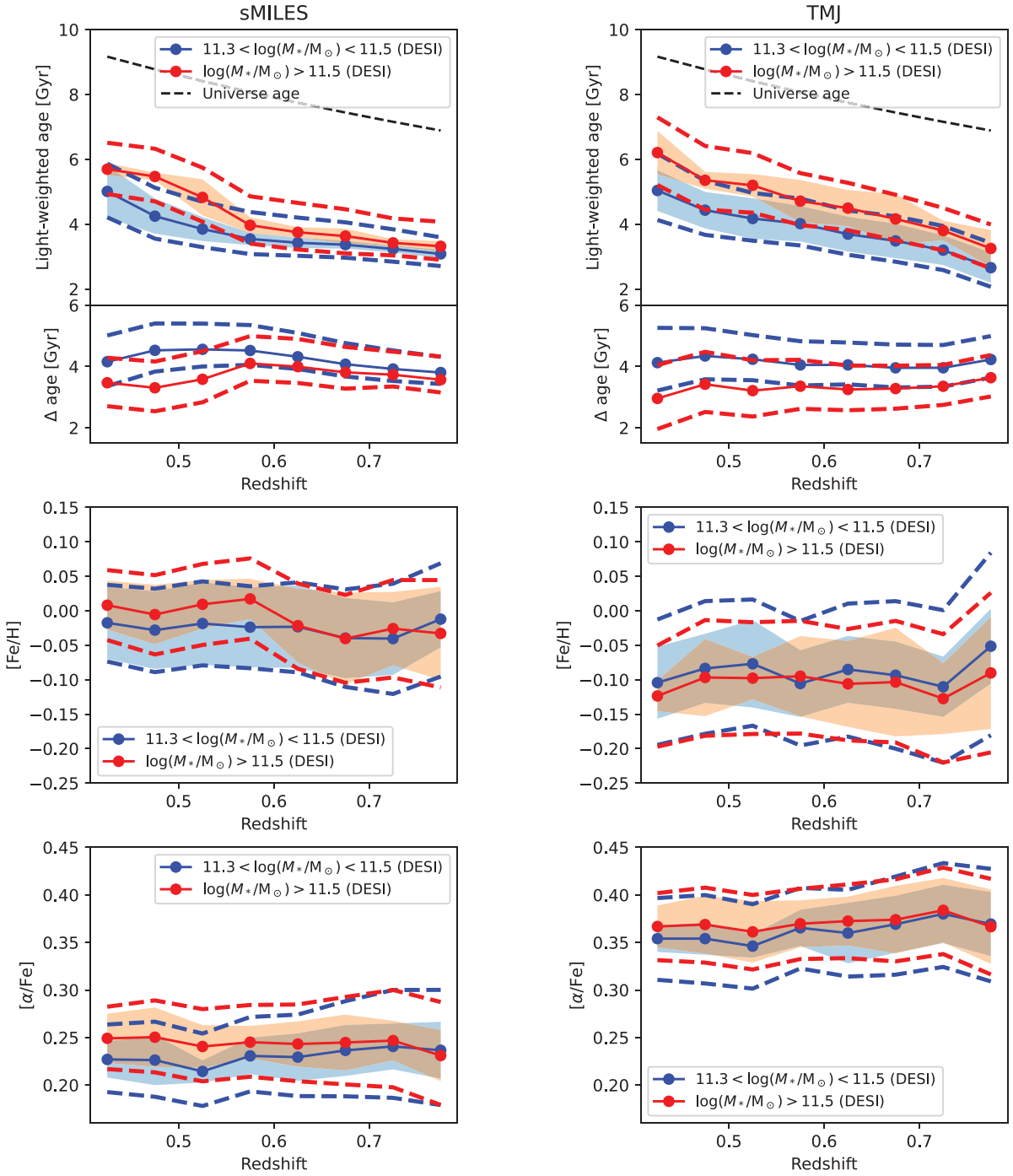


Figure 8. Evolution of the light-weighted age, [Fe/H] and [α/Fe] in the redshift range $0.4 < z < 0.8$ in the mass bins [$11.3 < \log(M_*/M_\odot) < 11.5$, $\log(M_*/M_\odot) > 11.5$]. Each top panel includes a sub-panel showing the difference between the age of the Universe and the light-weighted age. The three panels on the left show the results obtained using sMILES, while the three panels on the right show the corresponding results from TMJ. The data points represent the median value in each redshift bin, the dashed lines cover the typical uncertainties of the stacked spectra, and the shaded regions correspond to the intrinsic scatter within each bin. The dashed black line in the top panel represents the age of the Universe at each redshift.

al. 2026, for details). For this reason, we computed $[\alpha/\mathrm{Fe}]^{\mathrm{TNG}}_{\mathrm{sMILES}}$ using O, Ne, Mg, Si as α-elements, while $[\alpha/\mathrm{Fe}]^{\mathrm{TNG}}_{\mathrm{TMJ}}$ considering C, N, O, Ne, Mg and Si. We normalized the abundances using the solar reference value from M. Asplund et al. (2009) ($[\mathrm{Fe/H}]_\odot = -2.76$, $[\alpha/\mathrm{Fe}]_{\odot,\mathrm{sMILES}} = 0.81$, $[\alpha/\mathrm{Fe}]_{\odot,\mathrm{TMJ}} = 0.94$), since both TMJ and sMILES models express abundances in terms of logarithmic ratios relative to their adopted solar reference values.

Fig. 10 shows the evolution of the light-weighted age, [Fe/H] and [α/Fe] as a function of redshift for stacks of galaxies in the BOSS and DESI samples, alongside the parameters of the selected galaxies across the five TNG snapshots. The light-weighted age

Downloaded from academic.oup.com/mnras/article/548/4/stag766/8661535 by guest on 26 November 2026

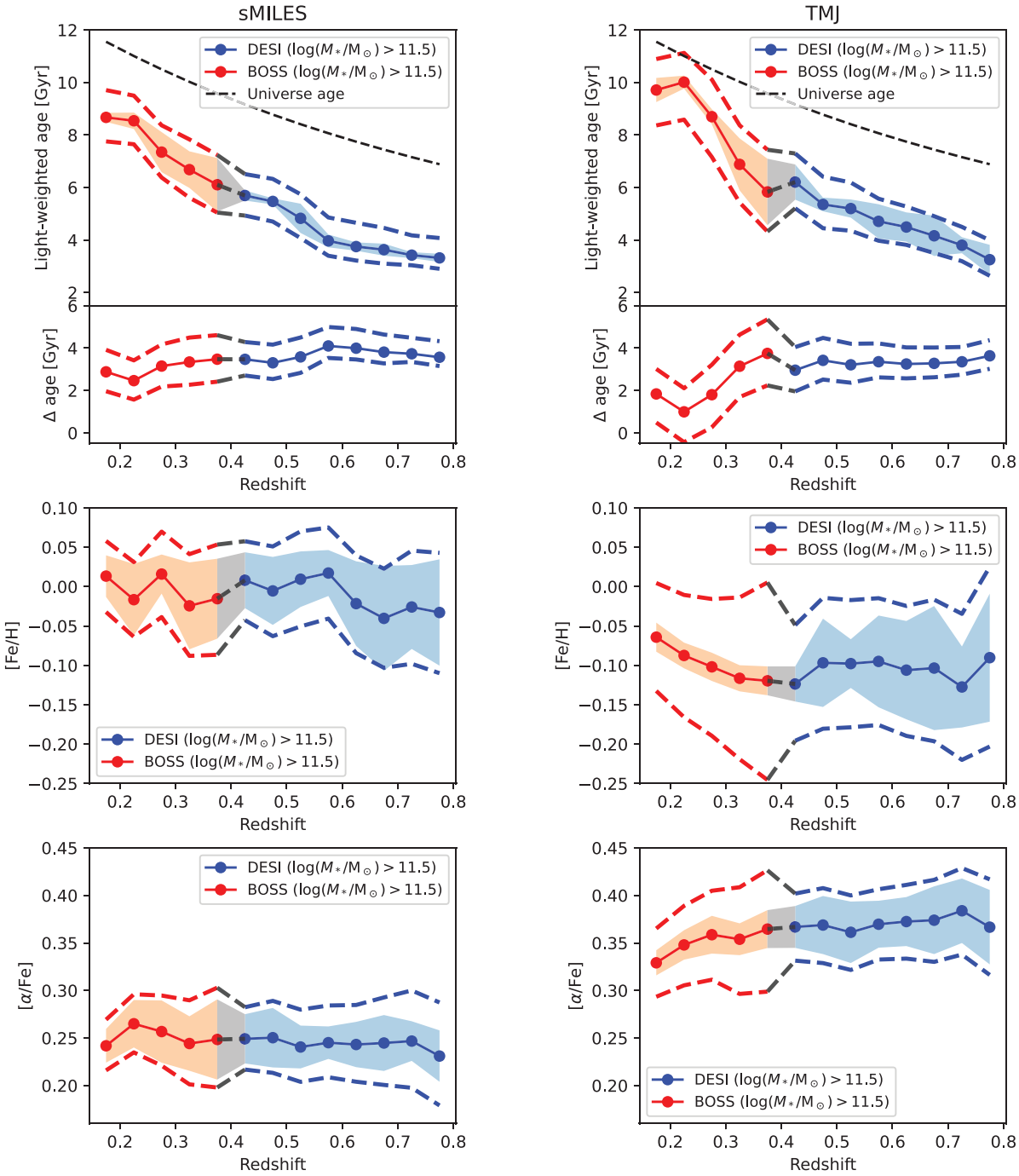


Figure 9. Evolution of the light-weighted age, [Fe/H] and [α/Fe] in the redshift range $0.15 < z < 0.8$. Each top panel includes a sub-panel showing the difference between the age of the Universe and the light-weighted age. The three panels on the left show the results obtained using sMILES, while the three panels on the right show the corresponding results from TMJ. The data points represent the median value in each redshift bin, the dashed lines cover the typical uncertainties of the stacked spectra, and the shaded regions correspond to the intrinsic scatter within each bin. The dashed black line in the top panel represents the age of the Universe at each redshift.

of TNG galaxies closely tracks the observed trends in the BOSS and DESI stacks, in both sMILES and TMJ analyses, with ages increasing from 4 Gyr to 9 Gyr towards lower redshifts, with an almost constant difference between the age of the Universe and the measured light-weighted age. This agreement lends support to the adopted selection of massive and quiescent galaxies in the TNG snapshots for the comparison. Both the observed and simulated galaxies show nearly flat trends in [Fe/H] and [α/Fe] towards lower redshift. However, we obtained different absolute values for all the stellar population parameters. In particular, simulated galaxies show lower values of [Fe/H] (difference of ~ 0.2 dex with sMILES, ~ 0.1 with TMJ) and higher values of [α/Fe] (difference of ~ 0.3 dex with sMILES, ~ 0.1 dex with TMJ).

Downloaded from academic.oup.com/mnras/article/548/4/stag766/8661535 by guest on 26 November 2026

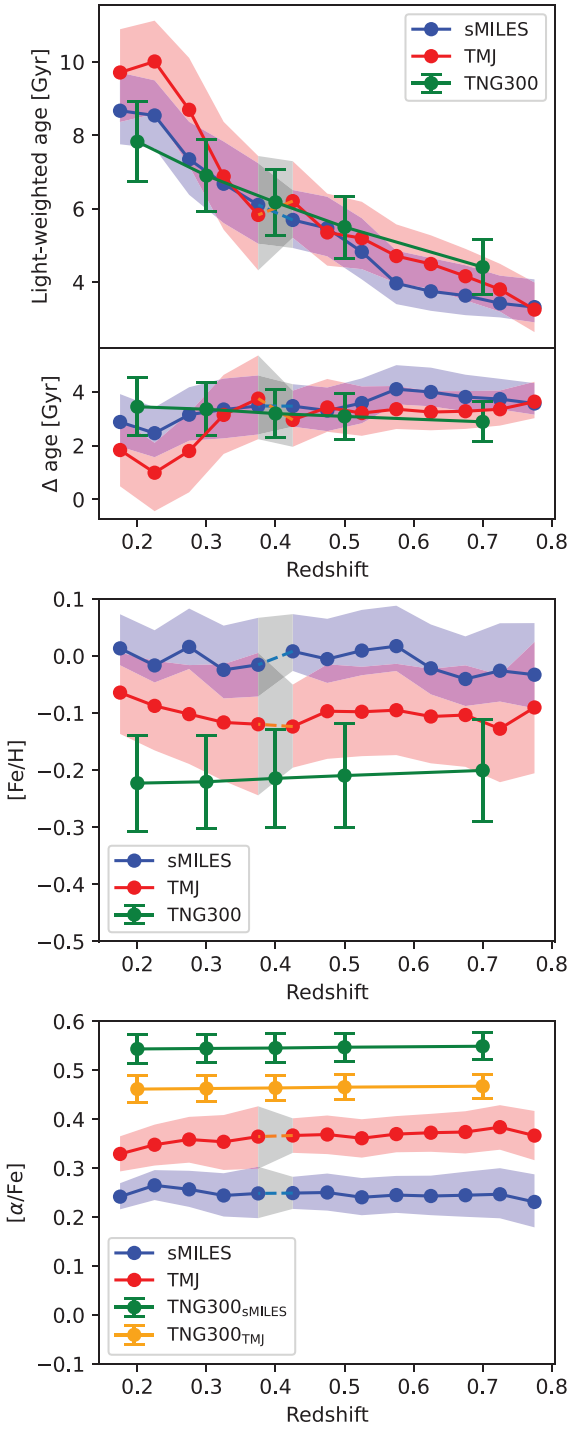


Figure 10. Evolution of the light-weighted age, [Fe/H] and [α/Fe] in the redshift range $0.15 < z < 0.8$. The top panel includes a sub-panel showing the difference between the age of the Universe and the light-weighted age. The blue (red) data points represent the median value in each redshift bin using sMILES (TMJ) models, and the shaded regions cover the typical uncertainties of the stacked spectra. The green data points and error bars are the median values and the dispersion of the stellar population parameters of the selected galaxies in five TNG300 snapshots. In the bottom panel the green (yellow) data points and error bars are the median values and the dispersion of the [α/Fe] from TNG galaxies considering the normalization given by the α-abundances of sMILES (TMJ) models. The dashed black line in the top panel represents the age of the Universe at each redshift.

6 DISCUSSION

The study of the age, [Fe/H] and the [α/Fe] abundance ratio of the most massive quiescent galaxies across the cosmic time provides valuable insights into the framework of galaxy formation and evolution. Thanks to the extensive spectroscopic data sets from the BOSS and DESI surveys, we have been able to investigate how the most massive and quiescent galaxy population evolves in the redshift range $0.15 < z < 0.8$. Moreover, thanks to the larger mass dynamic range of the DESI sample, we studied these quantities in two mass bins.

The DESI results reveal very consistent evolutionary trends for galaxies in the two mass bins, with the more massive systems showing slightly older ages, higher stellar metallicities, and enhanced [α/Fe] ratios across the redshift range $0.4 < z < 0.8$. Although these systematic differences are within the 1σ uncertainties, they are suggestive of a mild downsizing effect, in which the more massive galaxies formed their stars earlier and over shorter time-scales than their lower-mass counterparts (e.g. A. Gallazzi et al. 2005; D. Thomas et al. 2005; F. Fontanot et al. 2009). The measured intrinsic scatter is smaller than, or at most comparable to the uncertainties across both mass and redshift bins for all parameters, suggesting a homogeneous stellar population within the DESI stacked spectra.

As shown in Fig. 9, the most massive quiescent galaxies exhibit a passive evolution of the light-weighted age, with an almost constant offset from the Universe age. Our measurements also reveal no significant evolution in the global stellar metallicity of these most massive quiescent galaxies from $z \sim 0.8$ to $z \sim 0.15$, supporting the picture of their passive evolution.

A comparison between the sMILES and TMJ models shows that the derived stellar population parameters follow the same evolution trends in both cases. In particular, the [Fe/H] measurements using TMJ are systematically higher by around 0.1 dex with respect to sMILES results. For [α/Fe], our estimates effectively trace [Mg/Fe], as Mg is the dominant α-element feature driving the fit. Nonetheless, the absolute [α/Fe] values differ between sMILES and TMJ by around 0.1 dex. These differences are expected, since the two models rely on different chemical prescriptions and SSP construction. In particular, their distinct definitions of the α-element mixture naturally produce slightly different [Fe/H] and [α/Fe] values. The light-weighted ages derived with the two models are consistent with each other, despite the different stellar evolutionary prescriptions adopted. Indeed sMILES relies on BaSTI isochrones, while TMJ uses S. Cassisi et al. (1997), as well as additional model-specific recipes for the treatment of horizontal-branch and AGB phases. Despite these offsets in the absolute values of [Fe/H] and [α/Fe], the consistency of the evolutionary trends across the two model sets indicates that our main conclusions are robust to the choice of stellar population model. We can then proceed to compare these results with the predictions from cosmological simulations to assess whether current galaxy formation models reproduce the observed trends. Regardless of the absolute offset, the redshift evolution of [α/Fe] in TNG galaxies closely follows the observed trend obtained from the observations, both showing a constant trend across the entire redshift range. However, the [α/Fe] values predicted by TNG simulations for massive quiescent galaxies are systematically higher by ~ 0.2 dex than those derived from observations (J. P. Naiman et al. 2018; J.-H. Kim, S. Belli & R. Weinberger 2023). This result is confirmed by our results, for which we have a difference of ~ 0.3 dex from sMILES results, and ~ 0.1 dex from the TMJ ones. This

Downloaded from academic.oup.com/mnras/article/548/4/stag766/8661535 by guest on 26 November 2026

discrepancy likely originates from differences in nucleosynthetic yields and stellar population modelling. Indeed, according to J. P. Naiman et al. (2018), the offset may point to an overproduction of α-elements relative to Fe from core-collapse supernovae or a too low rate of Type Ia supernovae in the simulation physics. Regarding the [Fe/H] abundance patterns, previous works report broadly consistent or slightly higher values in the highest-mass bin in TNG than in their observational sample (J. P. Naiman et al. 2018; J.-H. Kim et al. 2023). However, these studies rely on small observed data sets, especially at high mass, making the comparison sensitive to the sample selection and aperture effects. With our larger and more homogeneous sample, instead we find that the observed [Fe/H] is higher (by ~ 0.2 dex with sMILES, ~ 0.1 dex with TMJ) than that of the simulated galaxies. Given the rapid quenching of the TNG galaxies, most stars form before the bulk of Type Ia supernovae explode, therefore much of the late-time iron enrichment does not get incorporated into new stars. The simulations therefore naturally predict slightly lower stellar [Fe/H] than observed.

Given the wide redshift range covered by our analysis, we can compare our results with previous studies of massive quiescent galaxies at different epochs. Numerous studies, based on different data and methodologies, consistently support a picture in which the highest mass quiescent galaxies evolve passively over the last 8 Gyr. Indeed, A. Gallazzi et al. (2014) found a strong similarity in the properties of quiescent galaxies at $z \sim 0.7$ and local quiescent systems for $\log(M_*/\mathrm{M}_\odot) > 11.5$, once accounting for passive evolution. Other works based on LEGA-C data (A. G. Beverage et al. 2023; D. Bevacqua et al. 2024), although limited to smaller samples, found that the formation epochs of the most massive galaxies at $0.6 < z < 0.75$ are consistent with those inferred for local galaxies. Stacking analyses at different redshifts further confirm the passive evolution of high-mass quiescent galaxies (J. Choi et al. 2014).

While the total stellar metallicity traces the overall metal content accumulated during star formation, the [α/Fe] abundance ratio provides the complementary information on the time-scales of that enrichment (D. Thomas et al. 1999). A key emerging result from both our results and simulations is that [α/Fe] shows no evolution across cosmic time for massive quiescent galaxies. J. Choi et al. (2014) and N. Leethochawalit et al. (2019), analysing composite spectra of massive quiescent galaxies up to $z \sim 0.5$, find very weak or no evolution in [Mg/Fe] compared to the local Universe. Similarly, LEGA-C massive quiescent galaxies at $z \sim 0.7$ show [Mg/Fe] ratios comparable to those of local massive early-type systems (A. G. Beverage et al. 2021; D. Bevacqua et al. 2023). These results indicate that the most massive quiescent galaxies observed at $0.15 < z < 0.8$ had already completed their star formation by $z \gtrsim 1.5$–2. Their uniformly high [Mg/Fe] ratios across this redshift range suggest that both the galaxies observed at $z \sim 0.8$ and those at $z \sim 0.15$ formed and quenched their stars at similar early epochs, implying rapid formation time-scales followed by passive evolution.

At higher redshift ($z \sim 1$–1.3), A. C. Carnall et al. (2019, 2022) reported slightly lower metallicities for galaxies with $\log(M_*/\mathrm{M}_\odot) > 11$, with an offset of ~ 0.2–0.3 dex below the local values. Their studies also found [Mg/Fe] ratios in massive quiescent galaxies comparable to those of local early-type systems, suggesting that the α-enhancement, and thus the short formation time-scales, were already established by $z \sim 1$. However, their measurements of stellar metallicity are consistent with an earlier evolutionary stage of the quiescent population. Between $z \sim 1.3$ and $z \sim 0.8$, that correspond to around 2 Gyr of cosmic time, the number density of quiescent galaxies with $\log(M_*/\mathrm{M}_\odot) > 11.5$ increases by a factor of ~ 4–5 (A. Muzzin et al. 2013). This implies that a large number of quenched systems joined the massive quiescent population during this period. These additions have been probably slightly more metal-rich but shared similarly high [Mg/Fe] ratios, producing a mild apparent evolution in metallicity while maintaining a roughly constant α-enhancement. This behaviour is indicative of a classical progenitor bias, where the growth of the quiescent population at lower redshift reflects the addition of recently quenched galaxies rather than the intrinsic evolution of the original quiescent systems. Further support for this interpretation comes from J. T. Mendel et al. (2015), who measured stellar population ages of massive quiescent galaxies at $1.5 < z < 2$. Their results, when compared with other studies at lower redshift, indicate that these high-redshift quiescent galaxies do not represent the bulk of the quiescent population observed at $z < 1$, but rather an earlier generation of massive systems that quenched rapidly and evolved passively thereafter. At $z < 1$, the stellar ages of massive quiescent galaxies are consistent with passive evolution, whereas at $1 < z < 2$ they appear to saturate to a young (~ 1 Gyr) age, reflecting the changing demographics of the average progenitor population. In contrast, from $z \sim 0.8$ to $z \sim 0.15$ our results show that the stellar population properties of the most massive quiescent galaxies remain remarkably constant, despite the nearly 5 Gyr of cosmic time and an additional increase in number density by a factor of 3–4 (e.g. A. Muzzin et al. 2013; M. Donnari et al. 2021). Our observational results then demonstrate that below $z \sim 0.8$ the progenitor bias is no longer significant, and the evolution of the massive quiescent population is largely explained by a simple, passively evolving, scenario. The galaxies added at later times not only preserve the trend of increasing age in a manner fully consistent with passive evolution, and show no change in the median metallicity or [α/Fe] with redshift, but also maintain a very similar spread of these quantities across the different redshift bins. This indicates that there is no detectable difference in the stellar populations of the galaxies progressively included at lower redshifts. Therefore, at $z < 0.8$, their evolution likely involved mostly minor dry mergers, which increased their stellar mass and size without significantly affecting the light-weighted age, [M/H] or [α/Fe] distribution. Consequently, while the build-up of the quiescent population between $z \sim 2$ and $z \sim 0.8$ is shaped by progenitor bias, at later times the most massive quiescent galaxies evolve passively, with structural growth dominating over further chemical or star-formation evolution. These findings naturally connect with studies of the local early-type galaxy population. In particular, D. Thomas et al. (2005) inferred that the formation of the total stellar mass in massive early-type galaxies was already nearly complete by $z \sim 1$, with subsequent stellar mass growth limited to low-mass systems. Our results directly confirm this prediction, painting a coherent picture in which the most massive quiescent galaxies evolve predominantly through passive ageing and minor structural transformations.

7 SUMMARY AND CONCLUSIONS

The analysis presented here provides the first homogeneous and continuous mapping of the stellar population properties of the most massive quiescent galaxies ($\log(M_*/\mathrm{M}_\odot) > 11.5$) across the last ~ 7 Gyr of cosmic time ($0.15 < z < 0.8$). This work has been made possible by the combination of the BOSS and DESI surveys, whose unprecedented spectral coverage and large sample size

Downloaded from academic.oup.com/mnras/article/548/4/stag766/8661535 by guest on 26 November 2026

provide the foundation for our analysis. By applying a homogeneous selection across the two data sets we were able to trace the evolution of the most massive quiescent systems across a wide redshift range. We measured trends of [Fe/H], [α/Fe], and light-weighted age of the most massive quiescent galaxies as continuous functions of redshift, and consistently fitting the same set of spectral indices at all redshifts. This methodological homogeneity removes inter-survey calibration biases that have so far limited direct evolutionary comparisons.

The resulting trends show no significant evolution in [α/Fe] and [Fe/H], and an age increase fully consistent with passive stellar evolution. These results are robust against the choice of stellar population models and analysis assumptions, and they are in excellent agreement with the predictions from IllustrisTNG, which similarly predict negligible evolution in the chemical properties of the most massive quiescent galaxies at $z \leq 0.8$. This remarkable stability indicates that, below $z \sim 0.8$, the evolution of the most massive quiescent population is genuinely passive. Galaxies that join the population at later times already exhibit stellar properties similar to those of systems in place at $z \sim 0.8$, suggesting that they formed the bulk of their stars at similarly early epochs. This implies that, below $z \sim 0.8$, the growth of the most massive quiescent galaxies is dominated by passive mass assembly through minor dry mergers rather than by the addition of freshly quenched systems.

Beyond confirming the qualitative expectations from previous snapshots and cosmological simulations, this work provides a quantitative characterization of the passive-evolution regime in a way that was previously unattainable. Indeed, it provides a quantitative benchmark for the passive evolution of the most massive galaxies, offering a solid empirical basis for future comparisons with hydrodynamical simulations and chemical-enrichment models. Forthcoming spectroscopic surveys will enable a further step forward by extending this analysis to individual galaxies and exploring the dispersion of stellar population properties as a function of stellar mass, environment, and cosmic time. Upcoming high-multiplex, wide-field instruments such as WEAVE and 4MOST facilities (R. S. Jong et al. 2019; S. Jin et al. 2024) will provide spectra for thousands of galaxies over wide spectral ranges and redshift intervals comparable to those of BOSS and DESI, but with S/N ratios high enough to derive detailed stellar population parameters on a galaxy-by-galaxy basis (e.g. 4MOST-StePS and WEAVE-StePS A. Iovino et al. 2023a, b). Moreover, the survey MOONRISE (R. Maiolino et al. 2020) will exploit the unique observing capabilities of MOONS at VLT to provide the data to extend this approach to $z \geq 1$, providing a direct view of the earliest phases of quenching and completing the empirical picture of massive galaxy evolution across cosmic time.

ACKNOWLEDGEMENTS

FRD, ML, and AI acknowledge financial support from INAF Large Grant 2022, FFO 1.05.01.86.16. FLB acknowledges support from INAF 2023 RSN1 Minigrant 1.05.23.04.01.

DATA AVAILABILITY

The observational data used in this paper are publicly accessible. BOSS data can be obtained from the SDSS Data Release Server (https://data.sdss.org/sas/), DESI data are available through the DESI Public Data Release portal(https://data.desi.lbl.gov/doc/), and IllustrisTNG data can be found at https://www.tng-project.org/data/downloads/TNG300-1/. The models and code used in this work rely on publicly available resources cited in the manuscript. No proprietary data were used.

REFERENCES

Asplund M., Grevesse N., Sauval A. J., Scott P., 2009, ARA&A, 47, 481
Barber T., Meiksin A., Murphy T., 2007, MNRAS, 377, 787
Bernardi M., Shankar F., Hyde J. B., Mei S., Marulli F., Sheth R. K., 2010, MNRAS, 404, 2087
Bevacqua D. et al., 2023, MNRAS, 525, 4219
Bevacqua D. et al., 2024, A&A, 690, A150
Beverage A. G., Kriek M., Conroy C., Bezanson R., Franx M., van der Wel A., 2021, ApJ, 917, L1
Beverage A. G., Kriek M., Conroy C., Sandford N. R., Bezanson R., Franx M., van der Wel A., Weisz D. R., 2023, ApJ, 948, 140
Buchner J., 2016, Stat. Comput., 26, 383
Buchner J., 2019, PASP, 131, 108005
Buchner J., 2021, J. Open Source Softw., 6, 3001
Bundy K., Leauthaud A., Saito S., Maraston C., Wake D. A., Thomas D., 2017, ApJ, 851, 34
Cappellari M., 2023, MNRAS, 526, 3273
Cappellari M., Emsellem E., 2004, PASP, 116, 138
Carnall A. C. et al., 2019, MNRAS, 490, 417
Carnall A. C. et al., 2022, ApJ, 929, 131
Cassisi S., Castellani M., Castellani V., 1997, A&A, 317, 108
Cervantes J., Vazdekis A., 2009, MNRAS, 392, 691
Choi J., Conroy C., Moustakas J., Graves G. J., Holden B. P., Brodwin M., Brown M. J., Van Dokkum P. G., 2014, ApJ, 792, 95
Dawson K. S. et al., 2013, AJ, 145, 10
de Jong R. S. et al., 2019, The Messenger, 175, 3
DESI Collaboration, 2016a, preprint (arXiv:1611.00036)
DESI Collaboration, 2016b, preprint (arXiv:1611.00037)
DESI Collaboration, 2026, AJ, 171, 5
Ditrani F. R., Longhetti M., Fossati M., Wolter A., 2024, A&A, 688, A89
Ditrani F. R. et al., 2025, A&A, 696, A116
Donnari M. et al., 2019, MNRAS, 485, 4817
Donnari M., Pillepich A., Nelson D., Marinacci F., Vogelsberger M., Hernquist L., 2021, MNRAS, 506, 4760
Eisenstein D. J. et al., 2001, AJ, 122, 2267
Eisenstein D. J. et al., 2005, ApJ, 633, 560
Eisenstein D. J. et al., 2011, AJ, 142, 72
Falcón-Barroso J., Sánchez-Blázquez P., Vazdekis A., Ricciardelli E., Cardiel N., Cenarro A., Gorgas J., Peletier R., 2011, A&A, 532, A95
Favole G., Montero-Dorta A. D., Prada F., Rodríguez-Torres S. A., Schlegel D. J., 2018, MNRAS, 480, 1415
Ferreras I., Weidner C., Vazdekis A., La Barbera F., 2015, MNRAS, 448, L82
Fontanot F., De Lucia G., Monaco P., Somerville R. S., Santini P., 2009, MNRAS, 397, 1776
Fontanot F., La Barbera F., De Lucia G., Pasquali A., Vazdekis A., 2018, MNRAS, 479, 5678
Gallazzi A., Charlot S., Brinchmann J., White S. D., Tremonti C. A., 2005, MNRAS, 362, 41
Gallazzi A., Bell E. F., Zibetti S., Brinchmann J., Kelson D. D., 2014, ApJ, 788, 72
Greggio L., Renzini A., 1983, A&A, 118, 217
Iovino A. et al., 2023a, The Messenger, 190, 22
Iovino A. et al., 2023b, A&A, 672, A87
Jafariyazani M., Newman A. B., Mobasher B., Belli S., Ellis R. S., Faisst A. L., 2025, ApJ, 986, 148
Jin S. et al., 2024, MNRAS, 530, 2688
Kim J.-H., Belli S., Weinberger R., 2023, MNRAS, 523, 849
Knowles A. T., Sansom A. E., Vazdekis A., Allende Prieto C., 2023, MNRAS, 523, 3450
Kroupa P., 2001, MNRAS, 322, 231

Downloaded from academic.oup.com/mnras/article/548/4/stag766/8661535 by guest on 26 November 2026

Kuntschner H., 2004, A&A, 426, 737
La Barbera F., Vazdekis A., Matteucci F., Spitoni E., Pasquali A., Martín-Navarro I., 2026, A&A, 705, 18
Leauthaud A. et al., 2016, MNRAS, 457, 4021
Leethochawalit N., Kirby E. N., Ellis R. S., Moran S. M., Treu T., 2019, ApJ, 885, 100
Longhetti M., Saracco P., 2009, MNRAS, 394, 774
Maiolino R. et al., 2020, The Messenger, 180, 24
Maraston C. et al., 2013, MNRAS, 435, 2764
Martín-Navarro I. et al., 2015, ApJ, 798, L4
Martín-Navarro I. et al., 2019, A&A, 626, A124
Maseda M. V. et al., 2021, ApJ, 923, 18
Matteucci F., Tornambe A., 1987, A&A, 185, 51
Mendel J. T. et al., 2015, ApJ, 804, L4
Muzzin A. et al., 2013, ApJ, 777, 18
Naiman J. P. et al., 2018, MNRAS, 477, 1206
Nelson D. et al., 2019, Comput. Astrophys. Cosmol., 6, 2
Oke J. B., 1974, ApJS, 27, 21
Osterbrock D. E., 1989, Astrophysics of Gaseous Nebulae and Active Galactic Nuclei
Parikh T., Thomas D., Maraston C., Westfall K. B., Andrews B. H., Boardman N. F., Drory N., Oyarzun G., 2021, MNRAS, 502, 5508
Pietrinferni A., Cassisi S., Salaris M., Castelli F., 2004, ApJ, 612, 168
Pietrinferni A., Cassisi S., Salaris M., Castelli F., 2006, ApJ, 642, 797
Pillepich A. et al., 2018, MNRAS, 473, 4077
Planck Collaboration, 2016, A&A, 594, A13
Poggianti B. M. et al., 2009, ApJ, 693, 112
Reid B. et al., 2016, MNRAS, 455, 1553
Renzini A., 2006, ARA&A, 44, 141
Sánchez-Blázquez P. et al., 2006, MNRAS, 371, 703
Santucci G. et al., 2020, ApJ, 896, 75
Scoville N. et al., 2007, ApJS, 172, 1
Springel V. et al., 2018, MNRAS, 475, 676
Thomas D., Greggio L., Bender R., 1999, MNRAS, 302, 537
Thomas D., Maraston C., Korn A., 2004, MNRAS, 351, L19
Thomas D., Maraston C., Bender R., De Oliveira C. M., 2005, ApJ, 621, 673
Thomas D., Maraston C., Schawinski K., Sarzi M., Silk J., 2010, MNRAS, 404, 1775
Thomas D., Maraston C., Johansson J., 2011, MNRAS, 412, 2183
Tinsley B. M., 1979, ApJ, 229, 1046
van der Wel A. et al., 2016, ApJS, 223, 29
van der Wel A. et al., 2021, ApJS, 256, 44
Vazdekis A. et al., 2015, MNRAS, 449, 1177
Werle A. et al., 2022, ApJ, 930, 43
Worthey G., Faber S., Gonzalez J. J., Burstein D., 1994, ApJS, 94, 687
Zhou R. et al., 2020, Res. Notes Am. Astron. Soc., 4, 181
Zhou R. et al., 2023, AJ, 165, 58
Zibetti S., Gallazzi A. R., Hirschmann M., Consolandi G., Falcón-Barroso J., van de Ven G., Lyubenova M., 2020, MNRAS, 491, 3562

APPENDIX A: CONSISTENCY BETWEEN BOSS AND DESI

We selected LRGs observed in both the BOSS and DESI surveys within the redshift range $0.35 < z < 0.6$ (for which we obtained 9854 galaxies), in order to test the consistency between DESI and BOSS spectra. We stacked the individual spectra in groups of 30 galaxies, using those matched between the BOSS and DESI data sets and we performed the same analysis described in Section 3. Fig. A1 shows the results obtained in the measure of light-weighted age, [Fe/H], and [α/Fe] for stacks of the matched galaxies in DESI and BOSS, using both sMILES and TMJ models. The results for age and [α/Fe] are within 1σ across the redshift range where BOSS and DESI overlap. By performing a weighted linear fit for each stellar population parameter as a function of redshift and comparing the resulting slopes via a Z-test, we obtained $Z < 1$ for each parameter and for both the sMILES and TMJ models. These results indicate that the derived slopes are statistically indistinguishable within 1σ. However, there is a systematic offset between the [Fe/H] measured from the DESI and BOSS spectra up to 0.05 dex in both analyses. The systematic offset in stellar metallicity that we found can be explained by the different fibre apertures used by the two instruments. BOSS fibres have a diameter of 2 arcsec, while DESI fibres are 1.5 arcsec, implying that BOSS spectra sample a larger fraction of each galaxy. Because massive quiescent galaxies are known to exhibit negative metallicity gradients, typically with $\Delta[\mathrm{M/H}]/\Delta \log R \sim -0.2$ to -0.4 (e.g. G. Santucci et al. 2020; S. Zibetti et al. 2020; T. Parikh et al. 2021), a larger aperture effectively includes a greater contribution from the outer, more metal-poor regions of the galaxies. Assuming a representative gradient of -0.3 dex/dex and the relative aperture sizes of DESI and BOSS (1.5 arcsec and 2 arcsec, corresponding to a difference of $\Delta \log \left(\frac{R_{\mathrm{BOSS}}}{R_{\mathrm{DESI}}}\right) \sim 0.12$), the expected metallicity difference is $\Delta[\mathrm{M/H}] \sim -0.04$ dex. This value is fully consistent with the observed offset (~ 0.05 dex) between the two data sets. This supports the interpretation that aperture effects, coupled with intrinsic metallicity gradients, are responsible for the discrepancy.

Downloaded from academic.oup.com/mnras/article/548/4/stag766/8661535 by guest on 26 November 2026

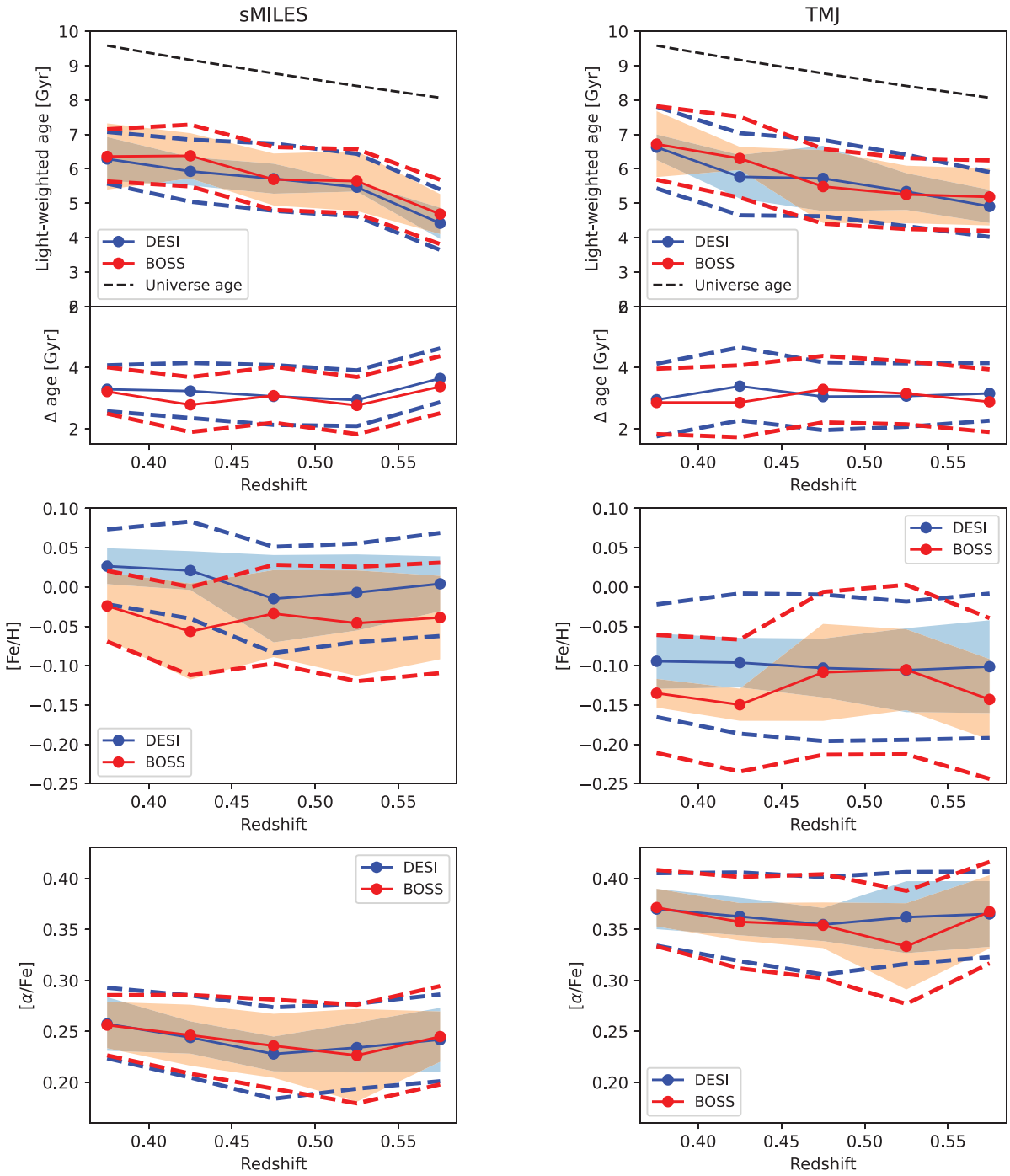


Figure A1. Light-weighted age, [Fe/H] and [α/Fe] in the redshift range $0.35 < z < 0.6$ for the matched DESI and BOSS stacked spectra. Each top panel includes a sub-panel showing the difference between the age of the Universe and the light-weighted age. The three panels on the left show the results obtained using sMILES, while the three panels on the right show the corresponding results from TMJ. The data points represent the median value in each redshift bin, the dashed lines cover the typical uncertainties of the stacked spectra, and the shaded regions correspond to the intrinsic scatter within each bin.

APPENDIX B: TNG300–TNG100 COMPARISON

We investigated potential differences of the stellar population parameters of massive quiescent galaxies ($\log(M_*/M_\odot) > 11.5$ and $\log(\mathrm{sSFR}) < -11$) within TNG300 and TNG100 in the five snapshots described in Section 5. Fig. B1 shows the light-weighted age, stellar metallicity and [α/Fe] in the redshift bins $z = [0.2, 0.3, 0.4, 0.5, 0.7]$ for TNG300 and TNG100. We found that galaxies in TNG300 have slightly older ages compared to the ones in TNG100, with an offset of around 0.5 Gyr, and well within the dispersion at each redshift. This is consistent with the reported effects of resolution on quenching time-scales. Indeed, galaxies in TNG300 quench slightly earlier than the ones in TNG100, and can explain the slightly older ages (e.g. M. Donnari et al. 2019; D. Nelson et al. 2019; M. Donnari et al. 2021). For the

Downloaded from academic.oup.com/mnras/article/548/4/stag766/8661535 by guest on 26 November 2026

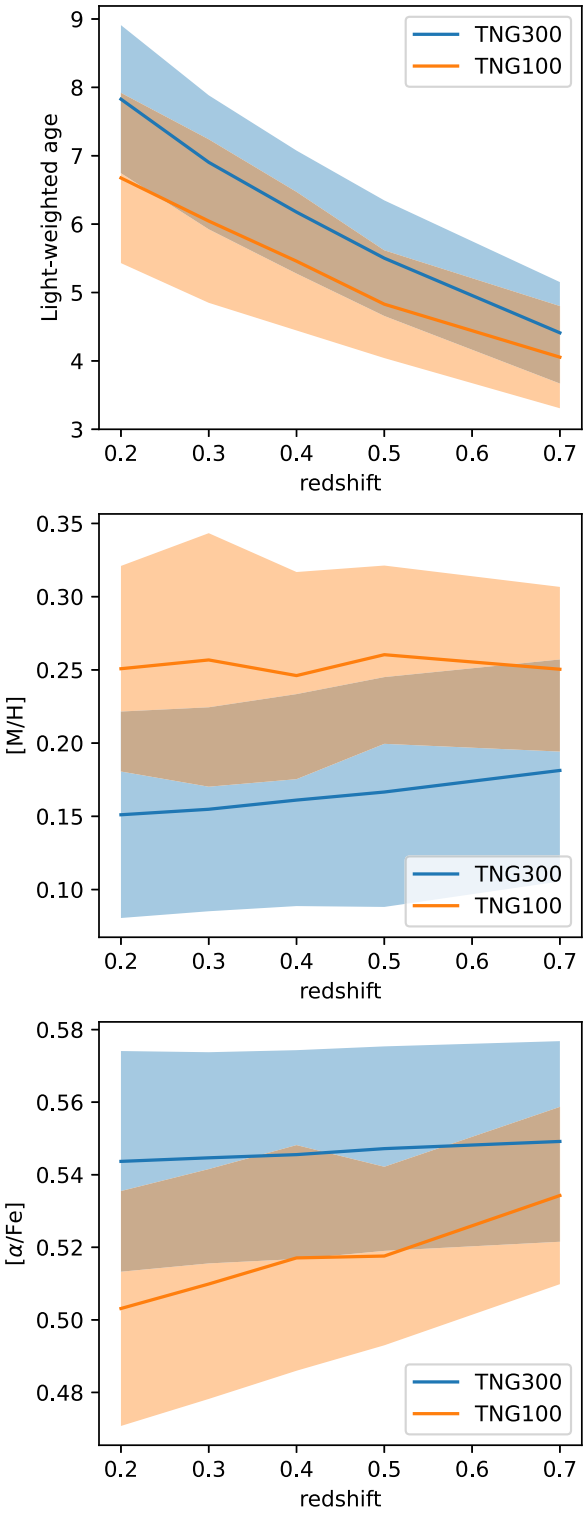


Figure B1. Evolution of the light-weighted age, [M/H] and [α/Fe] across the five redshift bins for galaxies in TNG300 (blue) and TNG100 (orange). The shaded regions represent the dispersion of each parameter within each redshift bin.

stellar metallicity, we estimated slightly lower values ($\approx 0.05 - 0.1$ dex) in galaxies from TNG300 with respect to the ones from TNG100.

Finally, we found that [α/Fe] are marginally higher ($\approx 0.02 - 0.04$ dex) in galaxies from TNG300 than the ones from TNG100. Despite these small differences, the trends and scatter of the stellar population parameters are consistent between the two simulations.

This paper has been typeset from a TEX/LATEX file prepared by the author.

Downloaded from academic.oup.com/mnras/article/548/4/stag766/8661535 by guest on 26 November 2026

© The Author(s) 2026.
Published by Oxford University Press on behalf of Royal Astronomical Society. This is an Open Access article distributed under the terms of the Creative Commons Attribution License (https://creativecommons.org/licenses/by/4.0/), which permits unrestricted reuse, distribution, and reproduction in any medium, provided the original work is properly cited.